ATLAS New Small Wheel sTGC Pad Efficiency and Signal Strength

by

Leesa Brown
B.Sc., University of Rochester, 2020

A Thesis Submitted in Partial Fulfillment of the
Requirements for the Degree of

MASTER OF SCIENCE

in the Department of Physics and Astronomy

ATLAS New Small Wheel sTGC Pad Efficiency and Signal Strength

by

Leesa Brown
B.Sc., University of Rochester, 2020

Supervisory Committee

Dr. Isabel Trigger, Co-supervisor
(Department of Physics and Astronomy & TRIUMF)

Dr. Robert McPherson, Co-supervisor
(Department of Physics and Astronomy)

ABSTRACT

The New Small Wheel (NSW) is the latest major upgrade of the ATLAS Muon Spectrometer and was installed during LHC Long Shutdown 2 between Runs 2 and 3. The NSW replaced the previous Small Wheels in the inner end-cap region and is composed of two technologies: MicroMegas and small-Strip Thin Gap Chambers (sTGC). The detector layers of the sTGC consist of wires centred between two cathode planes. One cathode plane is segmented into thin strips of constant width and the other into larger pads with variable sizes. From preliminary stand-alone tests and test beam results, the pads of the sTGC provide a coarse, fast trigger for the NSW and are able to distinguish muon signals in high-background environments.

Contents

List of Tables

List of Figures

STATEMENT OF ORIGINALITY

The results presented in this thesis were obtained in collaboration with many individuals affiliated with the ATLAS sTGC project. The New Small Wheel Collaboration is a large, international effort that required years of work to design, build, install, and operate the detectors. I was involved in the surface commissioning of one of the New Small Wheels. I helped install the readout and trigger boards (which are described in Section 3.5) in sector rim crates and connected readout cables and fibres to these boards.

During surface commissioning, I worked with Yotam Granov to create a comprehensive translation between various pad numbering schema. I utilized the translation information to convert the logical tower patterns created from simulated muon tracks into the pad numbering schemes used in the readout and triggering systems. I utilized and adapted pad display scripts created by Alex Tuna for the pad hit and efficiency maps shown in Chapters 4 and 5. I utilized the pad geometric information to calculate the polygons that describe the four layer logical towers. My analysis of the data from the surface cosmic ray tests (Subsection 4.1.1), in conjunction with the work by other members of the trigger commissioning team, helped find issues with the trigger firmware (incorrect pairs of logical towers on the two wedges) as well as timing issues with the readout system.

The pad heat maps and efficiency results from standalone runs during LHC Run 3 were used in conjunction with online results to detect and resolve an issue in the readout configuration file that was masking certain sTGC VMMs on every NSW sector. The configuration file was corrected in time for the dedicated end-cap muon alignment runs that were conducted with the ATLAS toroid magnets turned off.

I was involved in the setup and data collection for the sTGC test beam described in Chapter 5. The test beam required the efforts of many people, from the setup to having 24 hour shift coverage during the data collection period, as well as the other ongoing analyses. The Landau peak analyses described in that chapter are my own analyses in collaboration with Ksenia Solovieva and Isabel Trigger, with input and guidance from other members of the test beam analysis team.

ACKNOWLEDGEMENTS

I would like to thank my supervisor Dr. Isabel Trigger for all her guidance. In addition, I would like to thank my co-supervisor Dr. Robert McPherson.

I need to thank the sTGC trigger commissioning team, in particular Alex Tuna, Olga Zormpa, and Rimsky Alejandro Rojas Caballero. Without your efforts and data collection, the studies in Chapter 4 would not have been possible.

There are two individuals whose work I directly benefited from. Alex Tuna, your mapping scripts were vital to the completion of this thesis. Yotam Granov, thank you for your pad mapping work. The mapping spreadsheet you created was a massive help!

I am thanking my local supervisors at CERN, Gerado Vasquez and Artur Coimbra, for their guidance in my ATLAS authorship qualification project and recommending that I participate in the test beam.

The sTGC test beam group, organized by Margret Lutz and Estel Perez Codina, with Ksenia Solovieva, Prachi Atmasiddha, Siyuan Sun, Michael Schernau, Dennis Pudzha, and Stergios Tsigaridas and others all deserve a huge thanks.

Finally, I want to thank Juliette Martin for all your support.

Chapter 1

Introduction

Following the 2012 joint discovery of the Higgs boson [1][2] by the CMS and ATLAS [3] collaborations, experimental high energy physicists have been working to precisely measure Standard Model processes and couplings and search for hints of beyond Standard Model physics. The Large Hadron Collider provides an excellent laboratory for exploring many Standard Model processes such as the production and decay modes of W bosons and heavy quarks. Rare Standard Model (or beyond Standard Model) processes, like the simultaneous production of two Higgs Bosons, pose interesting physical and statistical challenges for the ATLAS Experiment. Such processes can have numerous decay modes that require multifaceted detection strategies. The relative rarity of these events requires the collection of a large amount of data before the threshold for discovery is reached. In order to increase the likelihood of observing events with interesting physics such as rare Standard Model processes, the beam luminosity (the proton-proton collision rate) must increase. Upgrades to the LHC are planned for 2026-2028 that will greatly increase its luminosity.

This coming upgrade of the LHC is known as the High Luminosity LHC (HL-LHC) and the accompanying increase in event rate will pose challenges for the LHC experiments. Major improvements in the ATLAS Muon Spectrometer began during the Long Shutdown 2 which began in 2018 and ended with the start of LHC Run 3 in 2022. To reduce the fake muon trigger rate and allow the muon trigger thresholds to remain at the relatively low momenta required to detect Higgs boson decays, the New Small Wheels were built and installed in the end-cap region in 2021, replacing the previous muon detectors in that region, the Small Wheels.

This thesis will discuss trigger tests and test beam results of one of the technologies, the Small Strip Thin Gap Chambers, of the New Small Wheel in the end-cap

region of the ATLAS Muon Spectrometer, with a focus on its functionality and efficiency as a muon trigger.

Chapter 2

The LHC and the ATLAS Experiment

CERN was founded in the 1950s to study atomic and nuclear physics [4], and has been a model for international scientific cooperation. As of 2022, CERN has 23 member states, two states with observer status (the US and Japan) and multiple associate member and participating non-member states, including Canada [5].

While CERN was founded to study nuclear physics, the scope of the organization has broadened to include many aspects of high energy physics. The Super Proton Synchrotron (SPS), now the final booster ring for the Large Hadron Collider (LHC), was used as a proton-antiproton collider for the discovery of the W and Z bosons. In the following years, the SPS became an electron-positron accelerator to serve as the final booster ring for the Large Electron-Positron Collider (LEP) which measured the W and Z boson masses and properties. In order to probe higher energies, the LHC, which accelerates and collides the much more massive proton, was built in the LEP tunnel and began operation in 2008 [6].

The Large Hadron Collider (LHC) is a 27 km circumference proton-proton collider with four main experiments located around the ring: ALICE, ATLAS, CMS and LHCb. A diagram of the LHC, the booster rings, and the LHC experiments is shown in Figure 2.1. The periods of LHC operation and data taking occurred over multiple years (LHC Runs), separated by Long Shutdown periods. The first period of ATLAS data collection, LHC Run 1, took place from 2009 to 2013 with proton-proton collisions with centre-of-mass energies of $\sqrt{s}$ =7 TeV and $\sqrt{s}$ =8 TeV used for the 2012 Higgs discovery. During the first Long Shutdown (LS) (2013-2015), upgrades to the

LHC and ATLAS were conducted, with the LHC providing proton-proton collisions with $\sqrt{s}$ =13 TeV during Run 2 (2015-2018) [7]. LHC Run 3 began July 2022, with collisions at 13.6 TeV, and is set to end in 2025 [8]. The luminosity (probability of collisions per unit time) of the proton beams has also increased over the years and is planned to increase further. ATLAS was initially designed for a peak instantaneous luminosity of $\mathcal{L} = 10^{34}$ cm^{-2} s^{-1} with the peak instantaneous luminosity reaching $\mathcal{L} = 2.1 \times 10^{34}$ cm^{-2} s^{-1} during Run 2 [9]. The LHC is expected to provide a sustained levelled instantaneous luminosity of $\mathcal{L} = 2 \times 10^{34}$ cm^{-2} s^{-1} during Run 3.

During Long Shutdown (LS) 3 (planned for 2026-2029 [10]), the LHC beam cavities and magnets will be upgraded in order to increase the instantaneous luminosity to $\mathcal{L} = 5 \times 10^{34}$ cm^{-2} s^{-1}. This future upgrade is known as the High Luminosity LHC (HL-LHC), and will ensure that LHC experiments like ATLAS will observe more interesting events (involving Higgs, W, Z, top quarks, etc.) and can further explore the Standard Model and exotic physics. Since the Higgs discovery, the LHC experiments have been working to precisely measure aspects of the Standard Model and search for new physics. With the increased energy and luminosity, the chance for interesting and groundbreaking discoveries is increased.

The LHC has 1,232 15 m long dipole magnets that bend the proton beam and 392 quadrupole magnets that are 5 to 7 m long and are used to focus the beams [7], as well as 16 radiofrequency (RF) cavities per beam that accelerate the protons [11]. The LHC beams are each structured with up to 2,808 bunches of protons grouped in 40 MHz bunches. Each bunch is filled with 1.2×10^{11} protons [12]. The 40 MHz frequency of the bunches crossing the centre of ATLAS forms one of the most important clocks for the experiment, the bunch crossing (BC) clock.

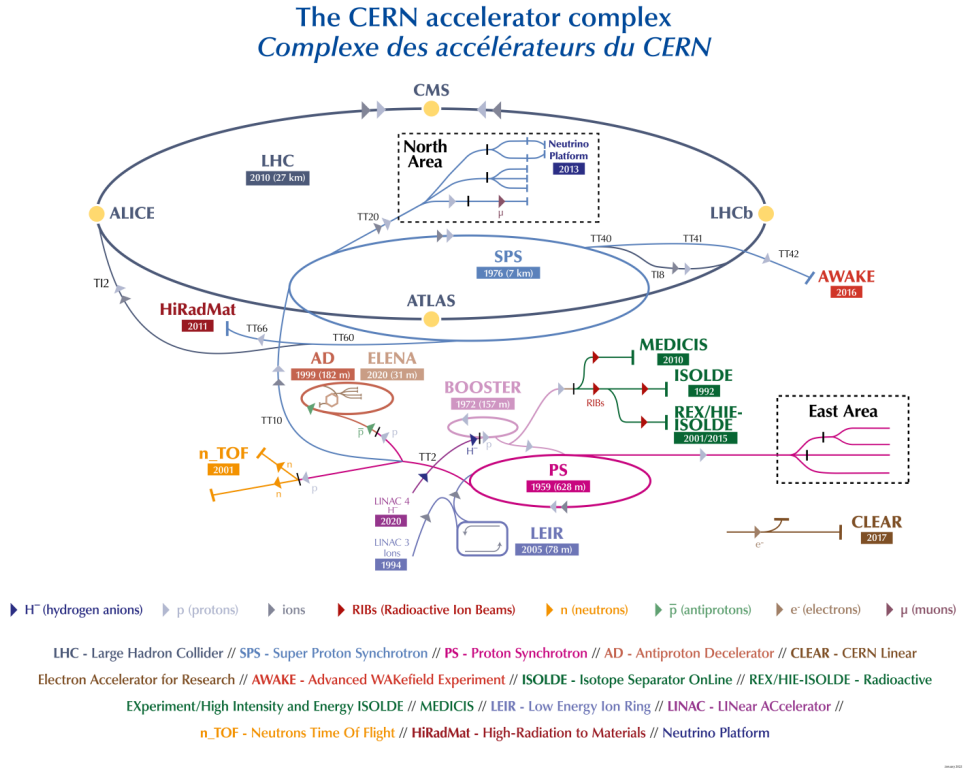

Figure 2.1: The CERN Accelerator Complex [6].

2.1 The ATLAS Experiment

The point where the two proton beams of the LHC are forced to cross, known as the Interaction Point (IP), is located within the centre of the ATLAS Experiment, 100 m underground near the main CERN site in Meyrin, Switzerland. ATLAS is 46 m long and 25 m in diameter, weighing over 7,000 tonnes. ATLAS consists of an inner tracker, electromagnetic and hadronic calorimeters, and the Muon Spectrometer. The inner tracker and calorimeters are contained within the three large toroidal magnet systems, with one at each end and one surrounding the barrel, see Figure 2.2.

2.1.1 ATLAS Coordinate System

The right-handed coordinate system used in ATLAS is defined by the proton beams, the IP, and the centre of the LHC, as shown in Figure 2.3, with the origin of the coordinate system at the nominal Interaction Point. The z-axis is along the beam pipe, pointing to side A of ATLAS (the side that faces Geneva, towards LHCb), and the

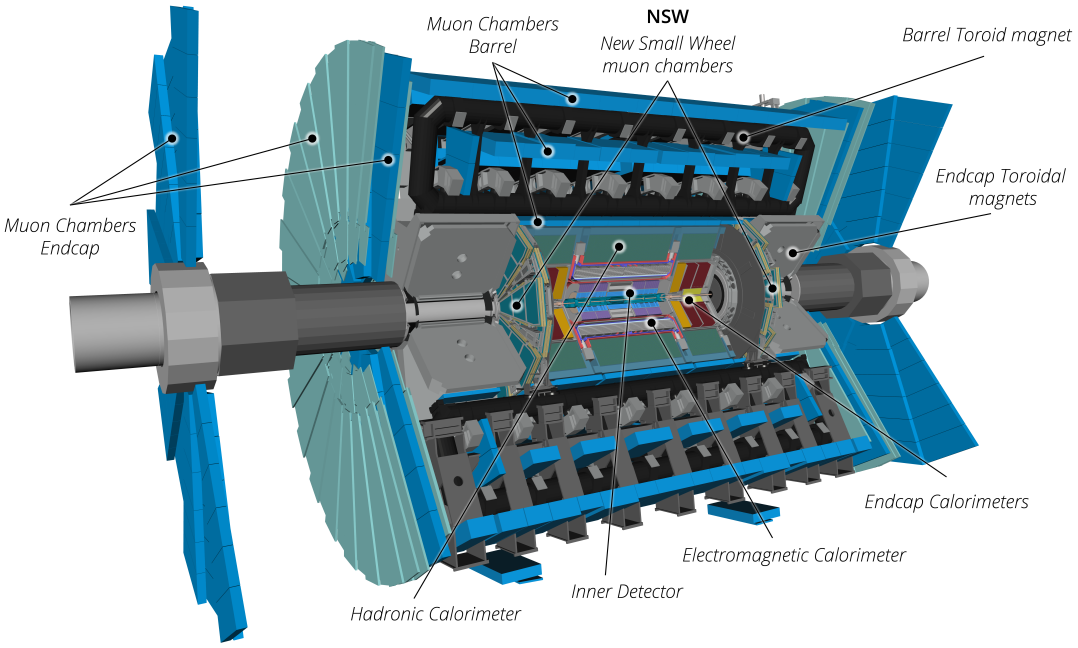

Figure 2.2: Cut-away view of the ATLAS Detector during Run 3 [9]. The inner subsystems and components of the Muon Spectrometer are labelled.

x-axis points from the IP to the centre of the LHC, with the y-axis pointing upwards. The transverse (x-y) plane uses polar coordinates with the radial coordinate r, and the azimuthal angle ϕ measured from the x-axis. Pseudorapidity is given by the polar angle θ measured from the positive z-axis as $\eta = -\log\tan(\theta/2)$ [13].

2.1.2 Components of ATLAS

ATLAS is a multipurpose experiment with multiple detector subsystems that are specialized in detecting particles within a given energy range and distance from the interaction point.

The ATLAS Inner Tracker, contained within a 2 Tesla (T) thin superconducting solenoid magnet, has three types of tracking detectors: Silicon Pixel detectors, Silicon Strip Detectors (SCT), and the Transition Radiation Tracker (TRT). The TRT uses straw tubes filled with gas and a wire in the centre for detection of charged particles. The Pixel and SCT detectors utilize solid state detection methods that measure electron-hole pairs produced by charged particles that pass through the detectors.

There are two forms of calorimetry measurements that are used within ATLAS. Electromagnetic (EM) calorimetry is the process of detecting electromagnetic cas-

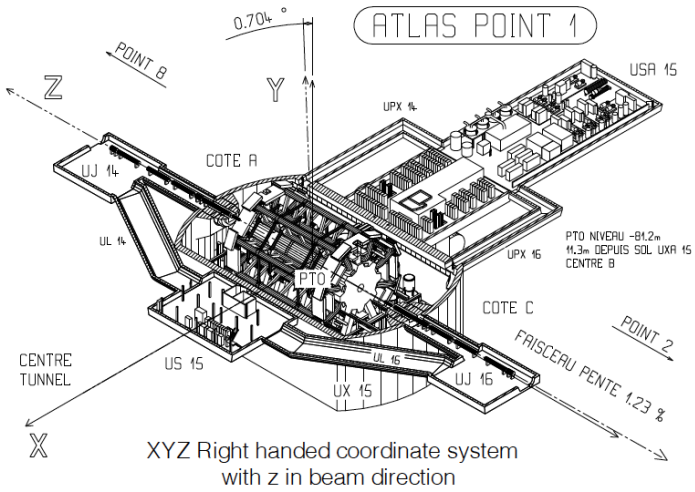

Figure 2.3: Illustration of ATLAS with the global coordinate system [3].

cades from high energy photons or electrons that are incident on a thick absorber. The incident particle produces a chain reaction through pair production (production of an electron and positron from a photon) and bremsstrahlung (emission of a photon by a charged particle) radiation. EM calorimeters in ATLAS are required to have a very fine granularity in order to give excellent measurements of electron energy, photon direction, and distinguish a prompt photon coming from the IP and two photons arriving close together from a π^0 decay.

Particles heavier than electrons are minimum ionizing at the multi-GeV energies required to escape the solenoid field and do not lose a large fraction of their energy to electromagnetic interactions. These particles will not be stopped by the EM calorimeter[1]. A much thicker calorimeter is needed to stop minimum ionizing hadrons by a combination of nuclear and EM interactions. Hadronic calorimeters are optimized to absorb the energy of hadrons through both electromagnetic and nuclear interactions [14], and measure the resulting energy deposition.

For both forms of calorimetry, the length of the resultant particle shower depends on the energy of the initial particle and properties of the calorimeter material (radiation length for EM calorimeter, nuclear interaction length for Hadronic calorimeter). Within ATLAS, liquid argon ionization (LAr) chambers are used for EM and hadronic calorimeters in the end-cap and inner barrel regions. Hadronic calorimetry

[1]As the length of the EM calorimeter is around a full hadronic interaction length, particles will begin their hadronic shower in the EM calorimeter. While the pions produced within ATLAS are minimum ionizing, pions interact strongly and lose a significant fraction of energy within the EM calorimeter.

is accomplished in the outer barrel region by iron and scintillator calorimeters (Tile calorimeters).

A large percentage of muons resulting from proton-proton interactions are high energy (with energies on the order of GeV). These muons are minimum ionizing and do not lose much energy within, and are not stopped by, the inner components of ATLAS. In order to capture as much information as possible about collision events, the Muon Spectrometer is vital.

2.2 The Muon Spectrometer

The ATLAS Muon Spectrometer (MS) (Figure 2.2) is composed of multiple detector technologies and is divided into two regions, the barrel and the end-caps. There are three large super-conducting toroidal magnets (one at each end-cap and one forming the barrel) with a magnetic field of approximately .5 T. The barrel toroid magnet has 8 coils, each with its own cryostat, which imposes a division of 16 sectors (in ϕ) onto the muon detectors in the barrel region. The end-cap region, consisting of the Small and Big Wheels which are separated by the end-cap toroids (each consisting of eight coils, housed in a single common cryostat), follows the 16 sector division. First-level (hardware) signals from the different technologies of the muon spectrometer are combined on a per-sector basis, where muon tracks that point at the IP, have sufficient energy, and meet other criteria are selected for the High Level Trigger (HLT), and track segments not meeting these criteria are vetoed.

The MS has excellent muon identification and tracking performance as well as good momentum resolution. The High Luminosity LHC poses challenges for the original MS design. As background rates increase with luminosity, the trigger is required to maintain its speed and efficiency while greatly improving its background rejection. Any new detector elements need to be radiation hard to ensure a long lifetime for the experiment.

The muon trajectory deflection in the bending plane of the magnetic field is measured by hits in the Monitored Drift Tubes. The triggers for the Muon Spectrometer in the barrel region ($|\eta|< 1$) come from Resistive Plate Chambers, and from the Thin Gap Chambers on the Big Wheel in the end-cap region ($1.0 < |\eta|< 2.7$) [15]. With the addition of the New Small Wheel (NSW), the small-Strip Thin Gap Chambers and MicroMegas provide track segments to confirm that triggering particles came from the IP.

The inner end-cap region is subject to a high background from low energy photons and neutrons originating from a prompt in-time background and a delayed out-of-time background. In-time background is generated by synchronous proton collisions within the same bunch crossing that triggered the ATLAS data taking mechanism. Long-lived thermal neutrons (with lifetimes of about 15 minutes) scatter within ATLAS and the surrounding cavern until decaying, producing an out-of-time background. The photon background originates from multiple sources and varies in time.

In addition, particle showers from the calorimeters in the end-cap region around the beam pipe result in charged particles that project radially into the end-cap toroids, which bend these particles onto exit trajectories that, upon reaching the Big Wheel, mimic the tracks of the high transverse momentum muons coming from the IP. This background has produced a high rate of fake triggers in the Big Wheel in Runs 1 and 2, and is discussed further in the next chapter.

With the HL-LHC, the Muon Spectrometer will be subjected to a higher background rate and more pile-up events. The Level-1 (L1) muon trigger will need to discriminate tracks from background (delta rays, neutrons, photons) and reject tracks that did not originate at the IP. The ATLAS Phase I upgrades to the Muon Spectrometer in advance of Run 3 were designed to be capable of handling a maximum instantaneous luminosity of 7.5 x 10^{34} cm^{-2} s^{-1}, with improved rejection of fake triggers in the end-cap region from the installation of the NSW.

2.2.1 Muon Spectrometer Technologies

The technologies used within the Muon Spectrometer are optimized for triggering, tracking, and momentum measurement, with the detector type and function varying with location within the MS. The location of various technologies is shown in Figure 2.4.

Resistive Plate Chambers

Each Resistive Plate Chamber (RPC) is effectively a large planar capacitor composed of 2 parallel high bulk resistivity electrode plates with a gap of 2 mm filled with a gas mixture[2] at atmospheric pressure, which serve as an ionizing target. The electrode plates are coated with a resistive varnish which, when high voltage is applied, estab-

[2]Gases in the RPC are Tetrafluorethane ($C_2H_2F_4$), Isobutane (Iso-C_4H_{10}), and Sulphur hexafluoride (SF_6) in proportions of 94.7%, 5.0%, and 0.3%.

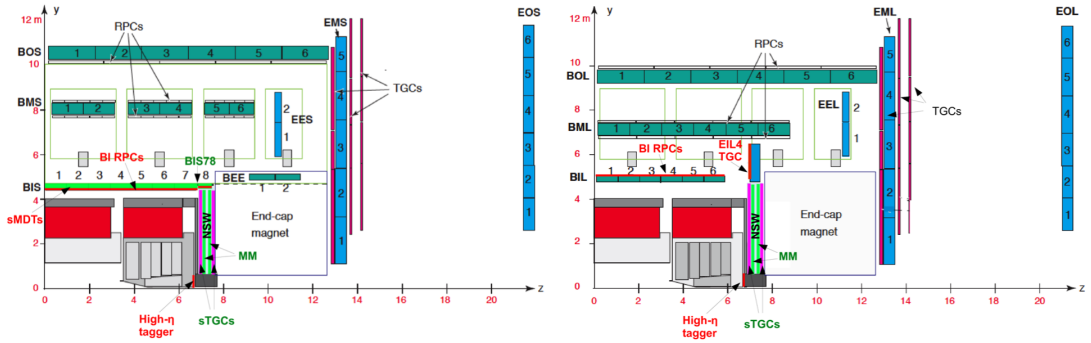

Figure 2.4: Cross-section view of small sectors (left) and large sectors (right) of the MS during Run 3 and planned Phase II upgrades [16]. The blue and dark green rectangles are MDTs. RPCs are located on both sides of the middle barrel (BM) MDTs and on one side of the outer barrel (BO) MDTs, as indicated by the arrows. TGCs form three Big Wheels at the middle end-cap (EM) station, also shown by arrows. The NSW location is indicated by the green labels and the pink and light green boxes. The Tile Calorimeters are represented by the red rectangles. Components that will be installed during LS3 are labelled in red.

lishes an electric field of 4.8 kV/mm across the gap that is capable of producing a prompt electron avalanche following the primary ionization. Each barrel sector has 3 layers of doublet chambers, which consist of 2 RPC gas gaps. The RPCs are read out by orthogonal strips on the plates with pitches ranging from 23 mm to 35 mm [15].

The RPCs have excellent spatial and timing resolution. In the non-bending plane, the RPCs provide muon triggers in the barrel region by coarse measurement and discrimination of muon transverse momentum (p_T), as well as fast, coarse tracking to identify hits related to muon tracks. The RPCs are able to trigger on single muons with minimum p_T of 20 GeV and can veto cosmic muons and search for long lived particles. In addition, the RPCs provide timing of hits relative to the bunch crossing and can measure the coordinates of a muon track with a resolution of 10 mm in z and ϕ [3].

Monitored Drift Tubes

High precision tracking of charged particles in the barrel region is done by the Monitored Drift Tubes (MDT). The MDTs are 30 mm diameter tubes with a wire in the centre that is held at a potential of 3270 V, and are filled with a gas mixture[3] held at a pressure of 3 bar. Muons and other charged particles ionize the gas and the freed

[3]MDT gas mixture is Ar, N_2, CH_4, in proportions of 91%, 4%, and 5% respectively.

electrons drift towards the wire, and the track position is measured with a resolution of 80 μm by a single drift tube. The MDTs are assembled on support frames with six or eight parallel layers of drift tubes (three or four layers per side of the support frame). Deformations of the tubes and support frames are monitored with built-in optical systems. The position monitoring combined with the multiple detector layers results in a high coordinate precision of about 35 μm [3]. In total, the MDTs cover an area of about 5500 m^2 and are currently located in the barrel and outer end-cap regions.

As drift time is determined by the diameter of the tubes (with a maximum drift time of 720 ns), smaller radius MDTs (sMDT) were added during LS1, during the 2016/2017 winter shutdown, and some MDTs were replaced with sMDTs during LS2. More MDTs will be replaced during LS3, as part of the ATLAS Phase II upgrade.

Thin Gap Chambers

The Thin Gap Chambers (TGC) are composed of two cathode planes, with fine wires (anodes) in the gap between the planes. One cathode plane is segmented into readout strips. The wires of the TGCs have wire-to-wire spacing of 1.8 mm and the cathode-to-anode spacing is 1.4 mm. The cathode planes are coated with a resistive graphite coating to let charge clear when there is a local pulse or spark. The TGCs are filled with a highly quenching gas mixture[4]. The gas is ionized by charged particles passing through the planes. The ionization electrons drift towards wires and produce avalanches which are detected as signals on the wires and induced signals on the strips. The n-pentane prevents sparking by absorbing photons that would produce additional avalanches. This allows for the chambers to be operated at higher voltages, which leads to larger gains. The strong electric field around wires and the small distance between the cathode planes reduces drift time for ionization clusters, which resulting in the slower drifting ions clearing relatively fast.

Thin Gap Chambers were utilized in the Big Wheels and the original Small Wheel. The TGCs measure the azimuthal coordinates of charged tracks, and the TGCs in the Big Wheels are used as a trigger in the end cap region. The MS has seven layers of TGCs in the middle end-cap (Big Wheel). These layers are grouped into one triplet wheel and two doublets.

After ATLAS began operation, an unexpected background was found. The Big

[4]The TGC gas mixture is CO_2 and n-pentane (n-C_5H_{12}) in proportions of 55% and 45%.

Wheel TGC triggers suffered from a high rate of fake triggers from (sometimes) slow charged particles that originate in the forward shielding surrounding the beam pipes and enter the toroid cryostats radially. The tracks get bent by the magnetic field, resulting in track segments in the Big Wheel that appear to originate from the IP yet are not from real muon tracks, which is shown in Figure 3.1. The technologies utilized in the original inner end-caps or Small Wheels (Cathode Strip Chambers and MDTs) were not fast enough to provide an efficient trigger in an environment that suffers from a high rate of 'leaks' from the calorimeters. In order to veto these fake triggers in the Big Wheel, the New Small Wheel was designed to trigger and provide track segments that can be matched with triggers and track segments from the Big Wheel. This motivated the design, construction, and installation of the New Small Wheel (NSW), a high-resolution, high efficiency, fast muon tracker, which is discussed further in the next chapter.

Chapter 3

The New Small Wheel

The New Small Wheels (NSW) are sets of detectors installed in 2021 and are the largest upgrade within ATLAS to date. The pair of muon end-cap detectors replaced the Small Wheels and introduced two technologies to ATLAS: MicroMegas and small-strip Thin Gap Chambers. Small-strip Thin Gap Chambers (sTGC) are a further development of the Thin Gap Chambers that are used in the Muon Spectrometer and allow high-granularity information from the inner end-cap region to be included in the trigger. With the new muon trigger in the inner end-cap region from the NSW, the Muon Spectrometer trigger will be able to veto more fake muon tracks at the hardware trigger level.

3.1 Motivation

As mentioned in the previous chapter, the Muon Spectrometer was impacted by a large, yet unexpected background from hits in the forward shielding that projected radially into the end-cap toroid cryostat, which produced track segments in the Big Wheels that appeared to point to the IP (Fig. 3.1). These background tracks were accepted by the Level 1 Muon Trigger and, at high luminosity, could saturate the trigger bandwidth with fake triggers. The New Small Wheel was designed and built to provide confirmation of triggers and track reconstruction in the inner end-cap region to reject this muon-like background, and thus avoid the need to pre-scale low-p_T muon triggers. The NSW is able to quickly and precisely trigger on track segments and send the trigger data to be compared with Big Wheel triggers within a latency of 1.08 μs following a collision. Once the track segments in both the NSW

and Big Wheels are matched, any track segments from the Big Wheel that do not have matching segments in the NSW can be vetoed and then the track angle can be used to reject tracks that did not originate from the IP. The NSW was designed to be capable of handling a maximum instantaneous luminosity of 7.5 x 10^{34} cm^{-2} s^{-1} and up to 200 pile-up events (simultaneous proton-proton interactions), while the expected maximum number of pile-up events the NSW will have to handle during Run 3 is 60.

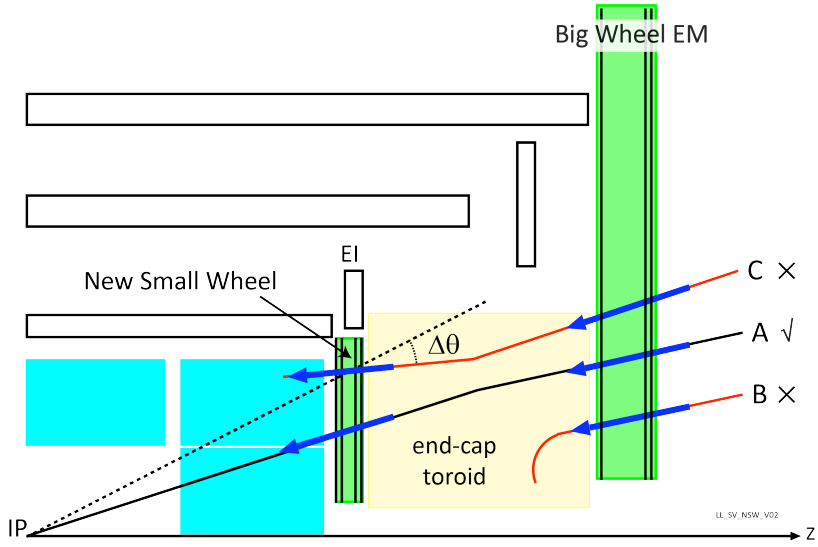

Figure 3.1: Examples of real and fake muon track segments [13]. Only Track A would be accepted as a trigger candidate in Run 3, as it was detected in the NSW and Big Wheel and the track points to the IP. Track C would be vetoed as the track segment measured by the NSW does not point back to the IP. Track B is an example of the fake muon trigger background observed in the MS during Runs 1 and 2, with a track segment in the Big Wheel but no corresponding track in the Small Wheel.

3.2 The New Small Wheel Layout

The New Small Wheel is composed of a supporting and shielding ("JD") disk and two detection technologies: MicroMegas (MM) and Small-strip Thin Gap Chambers (sTGC). The layout of the NSW sectors follows that of the Muon Spectrometer, with 16 sectors that provide full ϕ coverage via eight "large" sectors staggered with eight "small" sectors, as shown in Figure 3.2 . The sector numbering scheme is such that the large sectors are designated by odd numbers and the small sectors have even numbers. The sectors are kinematically attached to the NSW support

frame by spokes, which can be seen in Figure 3.3. The small sectors' spokes were mounted directly onto the JD disk and the large sectors were installed over the small sectors. Each sector has 16 detector planes with 4 multi-layers (wedges) of detectors. The wedges and technologies are arranged in the order sTGC-MM-MM-sTGC to maximize the distance between the sTGC layers on the two wedges. Each sTGC wedge is composed of 3 modules or quadruplets and the MM wedges are composed of 2 quadruplets, with each quadruplet having four detector layers. The composition and component breakdown of a sector are shown in Figure 3.4.

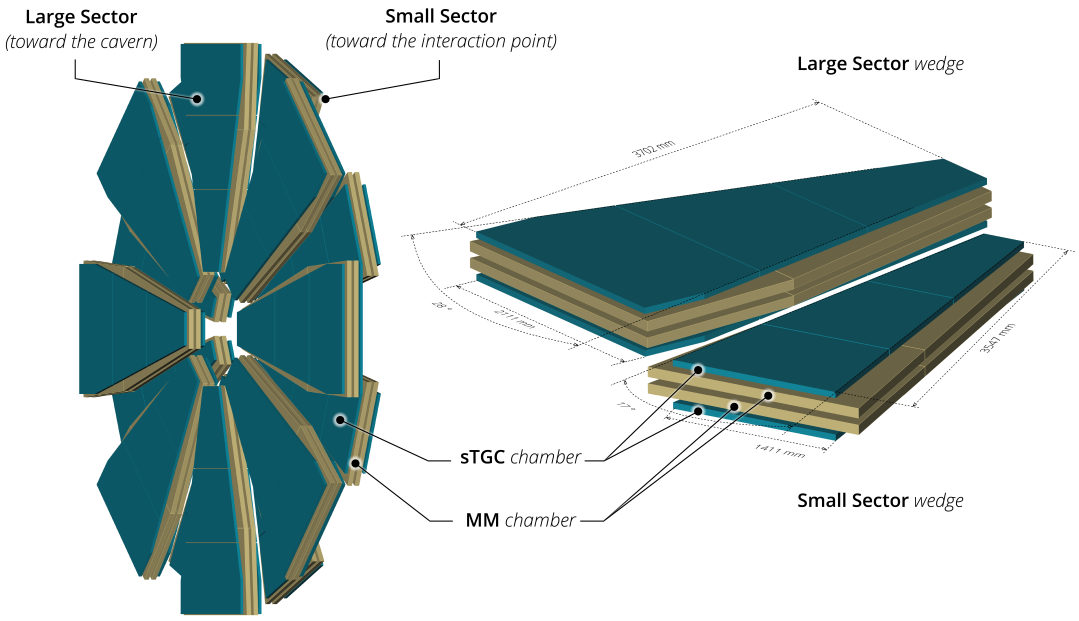

Figure 3.2: The sector arrangement of the NSW with each sector containing two sTGC wedges (blue) and MM wedges (yellow) [9]. The two sTGC wedges in a sector are referred to as the Confirm (outermost sTGC planes on the right of the diagram) and Pivot (innermost sTGC planes) wedges.

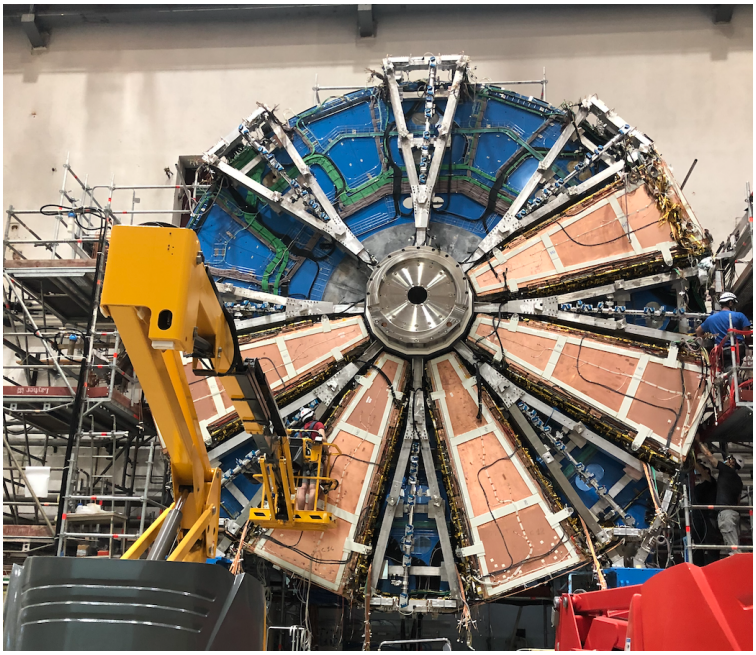

Figure 3.3: NSW C under construction, with 5 out of 8 small sectors installed onto the wheel. The wedge-shaped metal spokes for the small sectors are all present on the Wheel.

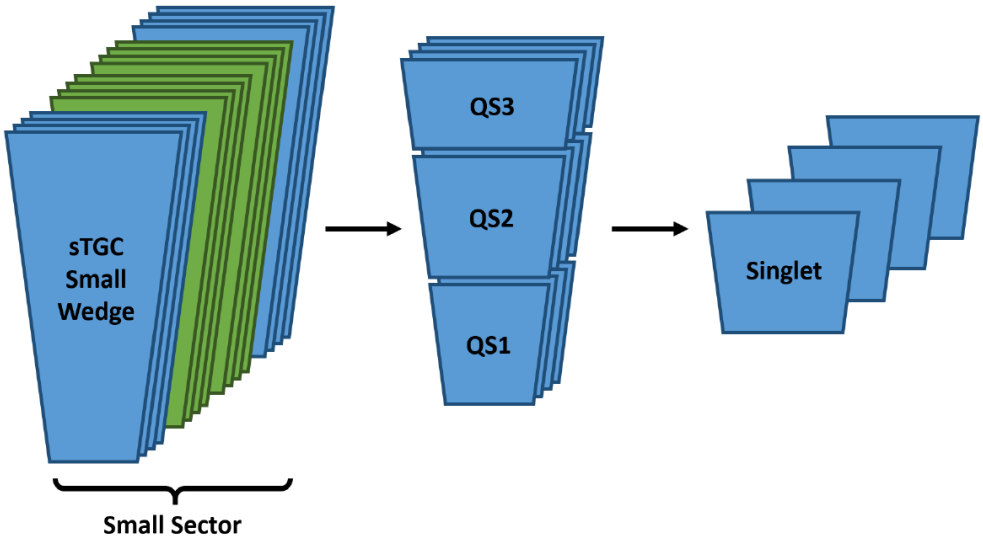

Figure 3.4: Constituent parts of a NSW sector [17].

3.3 MicroMegas

Micro-Mesh Gaseous Structure, or MicroMegas (MM), detectors, a type of micro-pattern gaseous detector, were developed in the mid 1990s and have allowed for the construction of thin, wireless gaseous particle detectors. The MicroMegas in the NSW consist of a planar (drift) electrode, a few millimetre wide gas gap that acts as a conversion and drift region, and a thin metallic mesh that creates an amplification region above the readout electrodes. The internal structure of a MM is shown in Figure 3.5. The MM are filled with an Ar, CO_2, and isobutane mixture at proportions 93%, 5%, and 2% respectively. MicroMegas were selected for the NSW for their fast precision tracking at a wide range of track angles.

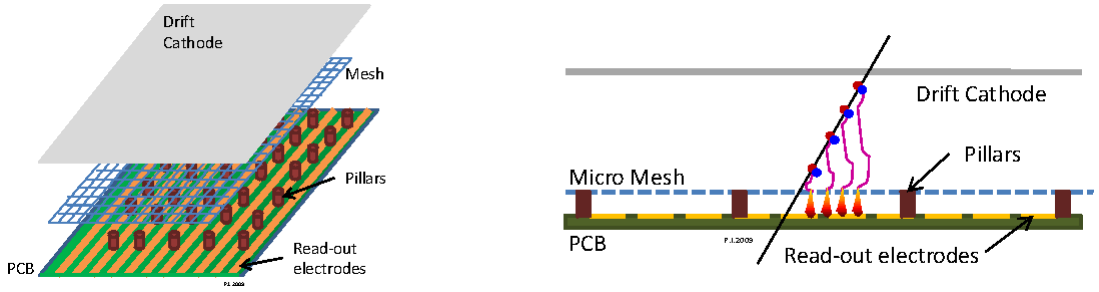

Figure 3.5: Diagram of the MicroMegas' internal structure (left) and an illustration of a signal from an angled charged track (right) [13]. The charged track ionizes the gas, and the freed electrons drift towards the MicroMesh, producing avalanches above the readout electrodes.

The readout electrodes were designed in a spark-protected resistive strip scheme to minimize the risk of sparking that is common with other MicroMegas detectors. The high voltage (HV) scheme was designed to further reduce the possibility of sparking, with a positive HV (490 to 520 V) applied to resistive strips and a negative HV (-300 V) applied to the amplification mesh.The high voltage value for the MM was chosen so that the electric field in the drift region is a few hundred V/cm while the electric field in the amplification region is approximately 40 - 50 kV/cm.

A charged track passing through the MM ionizes the gas, and the electrons drift towards the mesh while ions drift towards the drift electrode. Electrons arriving at the mesh produce avalanches, amplifying the signal directly above the readout electrodes. The electron drift time is relatively slow, taking about 10 ns, while the amplification process happens in a fraction of a nanosecond, resulting in fast pulses on the readout strips. The ions produced in the avalanche take about 100 ns to reach the mesh and

clear the charge. The fast evacuation of positive ions makes the MM suited to operate in the high particle flux environment that the NSW will be subject to during LHC Run 3 and HL-LHC.

3.4 Small-strip Thin Gap Chambers

Small-strip Thin Gap Chambers (sTGC) are multi-wire drift chambers consisting of a set of 50 µm gold-plated tungsten wires with a 1.8 mm pitch centred between two cathode planes, as shown in Figure 3.6. The cathode planes have a resistive graphite coating. One of the readout planes is segmented into fine strips with a 3.2 mm pitch and the other plane is divided into larger pads of varying sizes [13]. The gap between the planes is filled with a CO_2 n-pentane mixture identical to that used in the TGCs (the n-pentane to CO_2 ratio is 45:55). The major differences between the TGC and sTGCs are the much smaller strip pitch and the introduction of the pad plane, which is used for coarse, fast triggering. Each NSW has 23,328 pads, with large sectors containing 1,774 pads and the small sectors 1,142 pads.

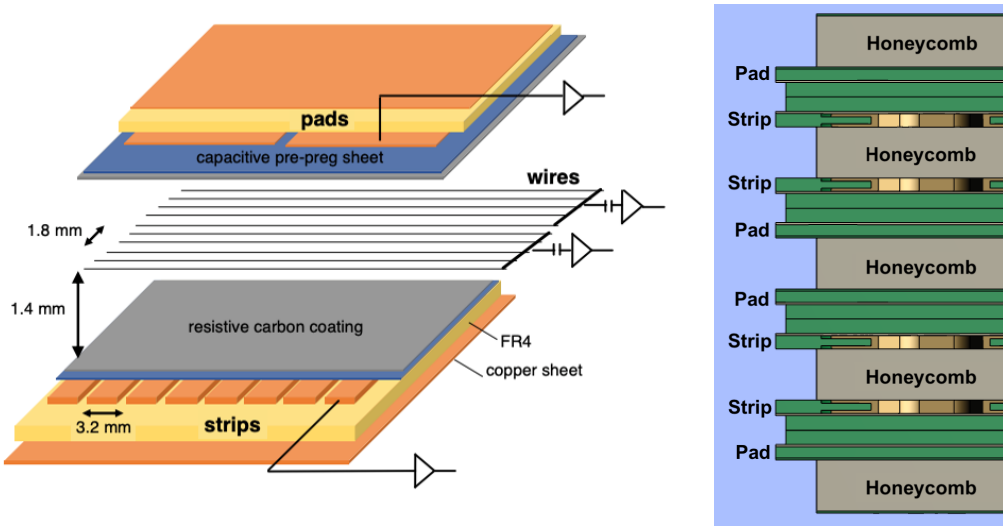

Figure 3.6: The internal structure of one sTGC gas volume (left) [9] and the layering of the four gas volumes in an sTGC quadruplet (right) [13].

Muons and other charged particles passing through sTGCs ionize the gas, producing electron-ion pairs. The freed electrons drift towards the anode wires in the centre of chamber, producing current. The signal is then amplified by the electrons creating avalanches near the wires, and inducing signals on the strips and pads. The

ions have a longer drift time, which in a high rate environment leads to the build up of drifting ions, creating a significant current that counteracts the electric field, producing long signal tails. To minimize this effect, the chambers have thin drift gaps, reducing maximum drift time. In a high rate environment, the build-up of drifting ions results in a constant current and a high minimum readout voltage.

As shown in Figure 3.7, the electric potential and thus the electric field is much lower half-way between two wires than it is close to the wires. When a muon passes exactly between two wires, it takes a long time for ionization electrons to drift into the higher-field region and be pulled towards a wire, producing an avalanche and signal. The signal from such a muon is delayed with respect to a typical signal. In order to minimize this effect, the wire positions are staggered by 0.25 wire-spacings between layers, which makes it unlikely that a muon would pass exactly between two wires on more than one of the four layers.

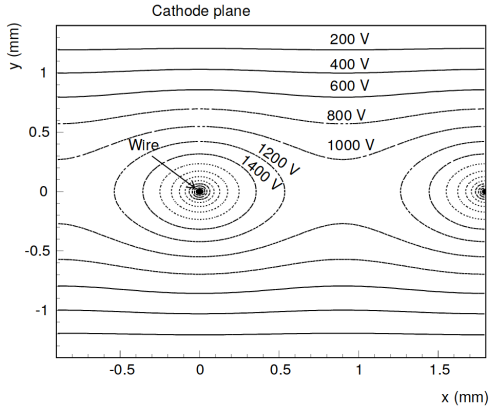

Figure 3.7: Diagram of the electric potential surrounding the wires for the sTGC [15]. The region between two wires has a significantly weaker electric field than the region surrounding a wire.

The local coordinate system used for the pads is based on the orientation of a wedge given in Figure 3.8, with the x-axis (labelled as "phi" in the diagram) oriented along the strips (parallel with the parallel edges of the modules) and the y-axis along the plane of the module, orthogonal to the x-axis (labelled "R"). The layer numbering scheme for studies using full sectors (a Pivot and Confirm sTGC wedge) begins with the layer closest to the Interaction Point (Layer 0) and increases in z moving from the IP (furthest is Layer 7). The three quadruplets in a wedge are numbered radially 1 to 3, beginning with the innermost quad[1]. The layer numbering scheme for an

[1]The innermost sTGC quadruplet has two high voltage sections, divided radially, which reduces

individual quadruplet ranges from 1 to 4, with Layer 1 closest to the IP.

The pad layers provide the initial hardware trigger for the NSW. A muon traversing the sTGC will produce hits in multiple layers of pads, and the pad hits provide coarse trigger information of the radial and ϕ coordinates of the muon track. The pad segmentation is staggered by half a pad in both x and y in the local coordinate system between layers of one wedge in order to produce smaller regions of overlapping pads that serve as the basis for the Pad Trigger. Pairs of overlapping regions on the two wedges are selected so that an IP-originating muon could traverse through the pads in both overlapping areas. The set of pads that compose these overlapping areas are referred to as a logical tower. The maximum distance between the Pivot and Confirm wedges places constraints on the angles of tracks that could produce multiple hits in a logical tower on both wedges. The Pad Trigger produces a trigger signal following coincident pad hits within a logical tower on three out of four layers of both the Confirm and Pivot wedges. The design of the logical towers allows for relatively large physical pads, reducing the number of individual readout channels needed per layer, as almost every pad is segmented into four logical towers, while providing an IP-pointing trigger. The trigger and readout chains are described further in the following section.

the currents in the high rapidity region [13]. Signals from the wires in the innermost section are not read out.

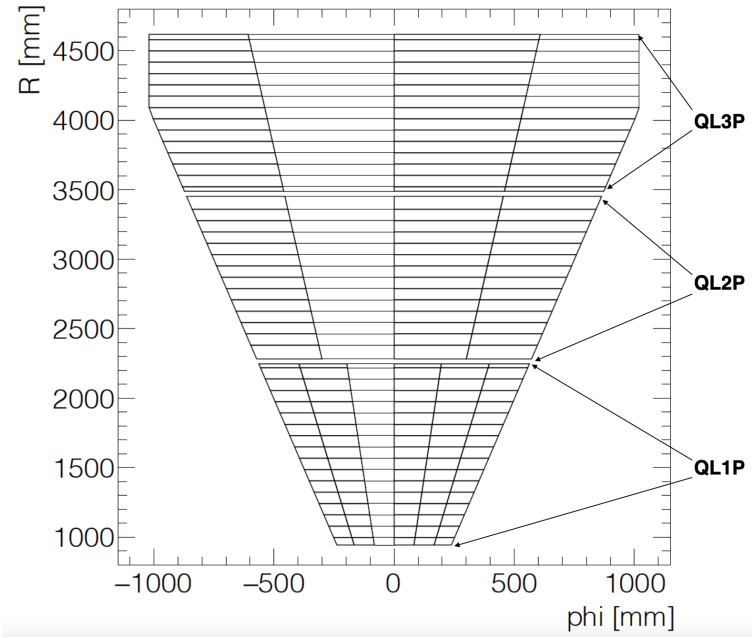

Figure 3.8: The outline of the first pad layer on the Pivot wedge in a large sector. The quadruplet division can be seen in the gaps between pad outlines and the quadruplets are labelled.

3.5 Triggering and Readout Systems

The on-detector electronics for triggering and readout are located on the front-end boards (FEBs), with off-detector electronics located on the NSW support frame (in the "rim crates") as well as in the ATLAS service caverns. There are 5,500 front-end boards which digitize and transmit signals from the 2.1 million MM and 360 thousand sTGC detector channels. While the detection and trigger systems for the two technologies vary, common frameworks and electronics were designed that serve the needs of both.

Due to its high rate environment, the NSW trigger needs to be fast and efficient. As discussed in Section 3.4, the pad cathode layer is a major difference between the TGCs and sTGCs and allows for the sTGCs to have a significantly higher trigger granularity. Coincident hits on multiple layers of pads are used for a fast and coarse trigger, determining a region of strips to be read; this is done by the Pad Trigger (PT) boards, located on the NSW support frame (JD disk). The strip signals are combined with signals from the MM to produce track segments that are combined with track segments from corresponding Big Wheel sectors in order to select muon trigger candidates. The pad trigger allows the sTGCs and in turn the NSW to be included in the

Level-1 trigger, reducing the fake trigger rate in the end-cap region by vetoing trigger candidates from the Big Wheel that do not have a matching track in the NSW. A diagram of the NSW trigger and readout chain is shown in Figure 3.9, and the various components are discussed in the next sections.

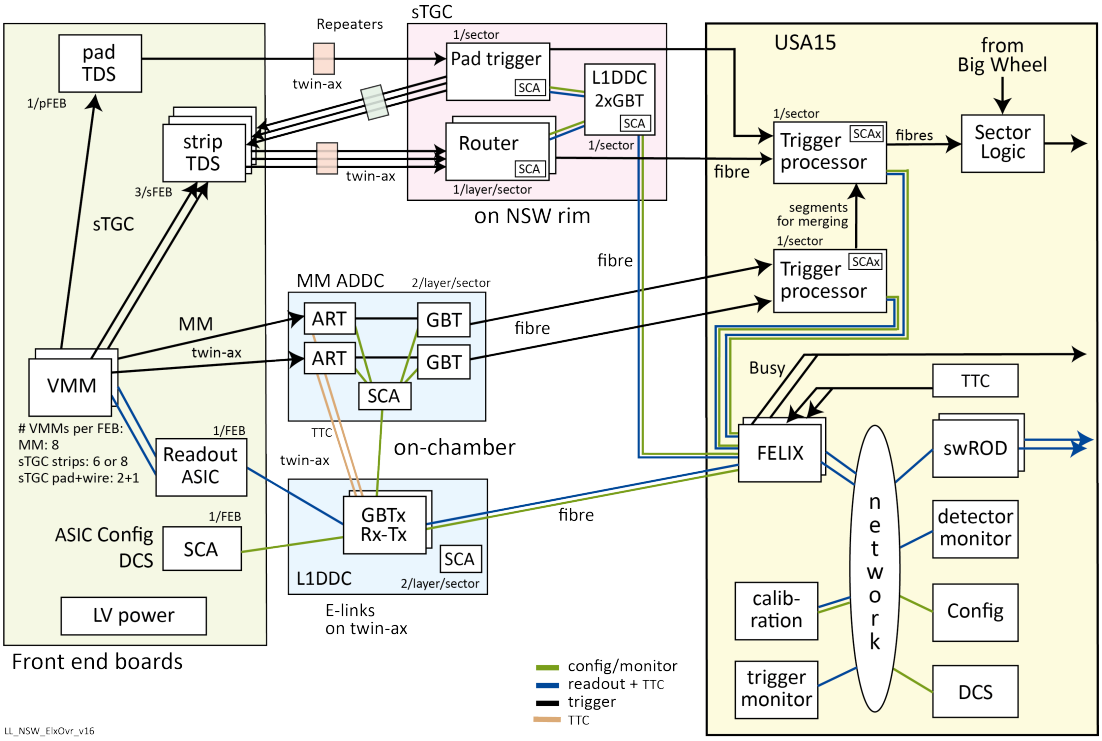

Figure 3.9: The NSW trigger and data readout path. The Front-end boards are located within the NSW. The boards in the pink box correspond to the electronics located within crates (with one crate per sector) on the NSW support frame. USA15 is one of the service caverns connected to the ATLAS cavern that contains support, electronics, and network equipment for ATLAS. Figure created by Lorne Levinson, ATLAS Experiment.

3.5.1 On-detector Components

The front-end boards (FEBs) of the sTGC and MM contain custom designed electronics that digitize and transmit signals and trigger information. The sTGCs have separate FEBs for the strips and the pads. Wires are arranged (typically) in groups of 20 and the signals from the wire groups are digitized and read out by circuits on the pad front end boards.

VMM

A custom Application Specific Integrated Circuit (ASIC) referred to as the VMM was designed to provide common, parallel readout and trigger paths for the front-end boards of the NSW detectors. As both the sTGCs and MMs require precision charge amplitude measurement for determining hit position and timing, a collaboration was formed in order to design and construct an ASIC to serve the needs of both technologies. The MM FEBs each have 8 VMMs. The sTGC strip FEBs have 6 to 8 VMMs to cover every strip channel, and the sTGC pad FEBs have 2 VMMs for the pad channels and 1 VMM for the wire groups.

Each VMM has 64 front-end channels that provide peak amplitude and time measurements with respect to the 40 MHz bunch crossing clock. The VMMs each have an amplifier-shaper-discriminator (ASD), peak detector, and 3 analog-to-digital converters (ADC) [18]. One of the ADCs is a 10-bit converter used to measure the precise charge information of a hit, another is an 8-bit time-to-digital converter (TDC) used to measure the time of the peak, and finally there is a fast 6-bit ADC. The 6-bit, or flash, ADC has a lower granularity compared to the 10-bit ADC but the significantly reduced conversion time makes it ideal for triggering purposes, while the 10-bit ADC has a conversion time of 200-380 ns depending on the operational configuration, during which time the channel is unable to record another hit (the channel's dead time). In comparison, the 6-bit ADC has a conversion time of about 25 ns [19]. The TDC and 6-bit ADC values are used by the sTGC trigger, while the 10-bit ADC values are used for precision track information.

Every channel has a baseline current that depends on global variables such as the high voltage, and channel-specific parameters like resistance and capacitance. Thresholds, the minimum peak height for signal to be considered as a "hit", are set above the baselines in order to prevent the signals from being swamped by background noise fluctuations. The thresholds on a VMM are set by a global 10-bit digital-to-analog converter (DAC) and individual channel 5-bit trimming DACs, which are adjusted to ensure all channels fire for the same minimum amount of charge [13].

When a channel has a signal that crosses its threshold, the peak detection circuit, which measures and stores the amplitude, is enabled. The time-to-amplitude converter (TAC) is a voltage ramp that starts at either the threshold crossing or the time of the peak and is stopped by the next bunch crossing [19]. The digital conversion process is shown in Figure 3.10. Two digital outputs from a VMM channel following

a signal are Time Detector Output (TDO) and Peak Detector Output (PDO). These are stored on the detector for a predefined period of time to allow for the signal to be read out following a trigger or discarded if no trigger is received. The peaking time, a user-controllable parameter, determines the length of time for charge integration, which is digitized and output as PDO. The pulse shape and the value of the PDO are affected by the semi-Gaussian shaper in the VMM that uses the peaking time as part of the shaping function which affects the shape and timing of the output signal.

Figure 3.10: Example of pulse and PDO and TAC conversion for a VMM operating in continuous mode [19]. The bunch crossing clock (CKBC) is shown with the time conversion process stopping at the end of a bunch crossing.

The VMM design allows for a multitude of operational choices. One setting of the VMM that is used in the sTGC strip trigger allows for reading out one or more channels immediately adjacent to a channel with a threshold-crossing signal, even if these signals are below the threshold. This "neighbours" feature of the VMM improves track reconstruction by allowing for relatively high thresholds while still being able to read out small-amplitude signals for charge clusters spread across several strips, resulting in higher coordinate precision.

Trigger Data Serializer

The front-end boards of the sTGCs have a companion ASIC, the Trigger Data Serializer (TDS), that serializes data from the pad or strip VMMs for transmission off-detector to the sector's trigger electronics boards located on the frame of the NSW, in the rim crate, with one crate per sector. Each TDS receives trigger data from two VMMs, which reduces the number of cables needed to transmit data off the detector. Following a bunch crossing, all pad hits are serialized and sent to the Pad Trigger located on the rim of the NSW (in a rim crate). The Pad Trigger searches for logical towers within the pad hits in the sector. If found, a signal is sent back to the strip FEBs to read out the corresponding strip signals. The pad trigger logic runs in parallel with the strip trigger and serialization, with strip hits being sent from the

VMM to the strip TDS to await a trigger from the Pad Trigger boards.

Data Transmission and Control

The need for a high speed, radiation hard data transmitter that is able to cope with the conditions of the LHC experiments led to a CERN group creating the gigabit transmission (GBT) ASIC chipset [20], which is significantly more radiation resistant than comparable commercially available chipsets. Off-the-shelf systems can be impacted by energetic (greater than 20 MeV) hadrons that cause single event upsets. In experiments such as ATLAS, transmission errors would significantly impact the data quality and would lead to loss of data. The GBT chipset is a radiation hard chipset that contains a 4.8 Gb/s serializer/deserializer ASIC, versatile optical transceiver and laser driver integrated circuit (IC), a pin diode receiver IC, and a slow control adapter (SCA). The SCA interfaces with several protocols, and is used in many components of ATLAS. The SCA handles slow control functions such as temperature and low voltage monitoring in addition to calibration and configuring of the VMMs and other on-detector NSW electronics. There is an SCA on every MM and sTGC front-end board.

Level-1 Data Driver Card

Hit data is combined from all VMMs on a FEB into a Level-1 (L1) data packet and serialized by the Readout Controller (ROC). The L1 data packet is transmitted to the L1 Data Driver Card (L1DDC), a high speed[2] aggregator board capable of communicating with a large number of FEBs. The L1DDC collects L1 data and monitors and transmits data to the network interface through a single bi-directional fibre link (e-link). The L1DDC communicates between the VMM and the GBT e-links that send signals to off-detector electronics [13], in addition to distributing Trigger, Timing, and Configuration (TTC) data from the network interface to the front-end boards. The sTGCs have L1DDCs located both on the detector and off-detector in the rim crates, with the on-detector L1DDCs receiving input from all 3 (strip or pad) FEBs in a layer. The sTGCs have one off-detector L1DDC per sector located within the rim crate that provides clock signals and configuration data to the on-detector L1DDC boards as well as transmitting trigger decisions to the network switch [9].

[2]The L1DDCs installed in the NSW are fully compatible with the ATLAS Phase II upgrade, and with a L1 trigger rate of 1 MHz.

3.5.2 Off-detector electronics and networks

Trigger signals from the pad TDS are sent to the Pad Trigger Board, located in the rim crate, with one per sector. If a coincidence of pad hits within a logical tower is found, a signal is sent back to the detector to select a region of strips for triggering. The Trigger Processor receives sTGC input from the Pad Trigger and the strip TDS, as well as the MMs, and merges the data from all three to compute track segments. The Trigger Processor uses the trigger data from the sTGC strips to calculate centroids of charge distributions spread across multiple readout strips, which gives the radial coordinate for the track. The ϕ coordinate comes from the triggering pad tower. Different calculation methods are used on the MM data to calculate centroids and track segments.

The Front End LInk eXchange system (FELIX) is the universal slow control and readout system for all ATLAS Phase I and II upgraded detectors, and acts as the network switch, communicating with the detector control system, configuration, and calibration databases. It is vital for the pre-data collection stages of calibration and for operations in addition to serving as the back-end data acquisition (DAQ) system for the NSW.

The software Readout Driver (swROD) captures all readout data that is broadcast to the network, combining packets from the multiple FELIX that correspond to a single event, and writing data to disk (for standalone runs) or propagating events to the ATLAS High Level Trigger (HLT).

3.6 NSW Production, Integration, and Commissioning

The electronics and detectors for the NSW were produced at numerous facilities around the world. The sTGC modules were first built as half-gaps, with the graphite layer sprayed onto the individual cathode boards and polished to a uniform resistivity. The wire supports and high voltage frames were then glued on. Wires were wound onto pairs of pad cathode boards, mounted back-to-back on a winding machine before the two layers of gas volumes were assembled. The pairs of two layers were then combined to form the four layer quadruplets. The assembly of sTGC quadruplets occurred at 9 sites in 5 countries. The list of countries with the sTGC modules they produced are given in Table 3.1. At these production facilities, the modules

underwent quality control tests, including measuring signals triggered by cosmic rays in an external scintillator.

Country	Quadruplet
Canada	QS3P, QL2P, QL2C
Chile	QS1P, QS1C
China	QS2P, QS2C
Israel	QS3C, QL1P, QL1C
Russia	QL3P, QL3C

Table 3.1: National distribution of sTGC production. The naming scheme of a quadruplet begins with Q, followed by size: either S for a Small quadruplet or L for a Large one. Next is the module number (1 being radially innermost, 3 outermost) followed by the wedge the module will belong on: Pivot (P) or Confirm (C).

The completed quadruplets were shipped to CERN, where the quadruplets were subjected to irradiation tests at the CERN Gamma Irradiation Facility (GIF++). Quadruplets that passed the reception tests were prepared for integration.

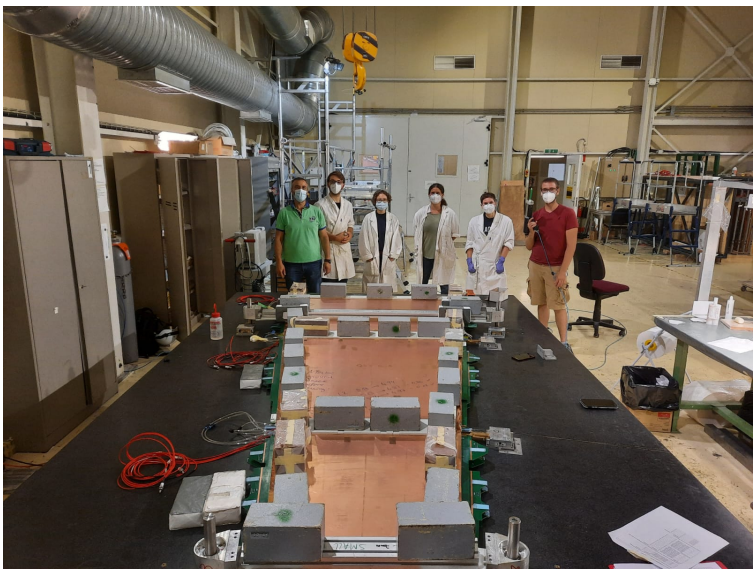

Figure 3.11: A small wedge on the granite table in the sTGC CERN clean room. The connecting fibreglass frame had just been glued onto the quadruplets, forming a wedge. Photo courtesy of Estel Perez Codina.

The integration of the three quadruplets that form a wedge occurred in the sTGC clean room in Building 180 at CERN. The three quadruplets were precisely placed against positioning pins on a granite table and long bands of radiation hard fibreglass were glued onto the quadruplets, joining them together. A small wedge with a recently

glued fibreglass frame is shown in Figure 3.11. After the glue had dried at least a day, a vacuum turning tool was used to flip the wedge over so that the other side could be glued. With both sides glued, the new wedge was removed from the granite table and high voltage cables were installed.

The wedges were tested for long-term high voltage stability (while filled with the n-pentane CO_2 gas mixture). The wedges underwent X-ray tests to measure the as-built location of the strips. Following the HV tests, the rest of the cabling and electronics were installed. The noise levels and response of the front-end electronics to pulses were tested with the wedges filled with CO_2. Following successful tests, wedges were moved to the adjacent building where the NSWs were constructed and two sTGC wedges were integrated with pairs MM wedges to form a sector. After the new sector was inspected, it was lifted by the ceiling crane and positioned and mounted onto the NSW. A large sector being lifted and positioned is shown in Figure 3.12. Once the sector was mounted, cooling and gas services were connected followed by electronics (low and high voltage and triggering cabling) and readout connections.

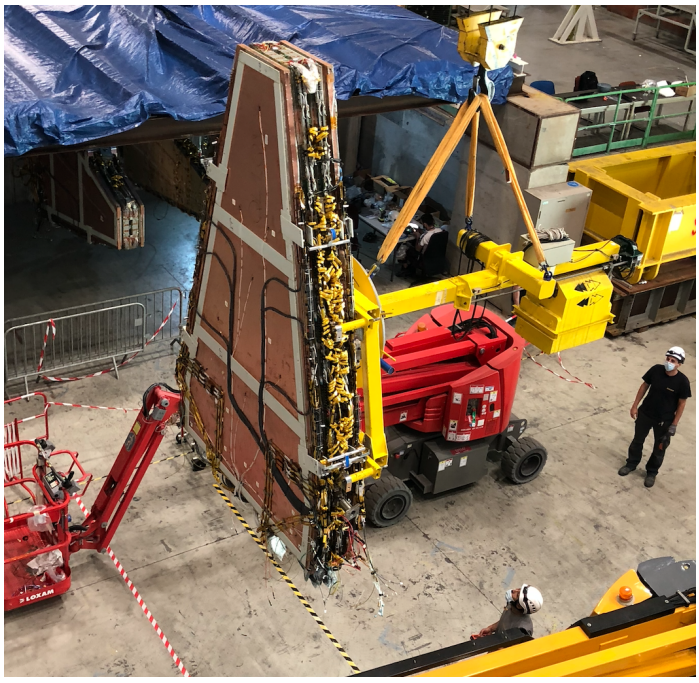

Figure 3.12: A large sector (C13) being lifted by a ceiling crane with a special turning tool in order to be installed onto the wheel. Other assembled sectors can be seen in the background, under the blue tarp covering.

Following service connections and cable routing, the sTGC commissioning team installed the off-detector electronics (Pad Trigger, Router, and L1DDC boards) in the

sector's rim crate (on the JD). Once cables and readout fibres from the sector were connected to the appropriate boards, connectivity tests were conducted to ensure all connections were correct and working, and that data was being transmitted accurately off the detector. The noise and pulse tests were repeated to ensure that no major changes or damage occurred during the installation process. These tests ensured that the trigger and readout system were functioning and properly commissioned. During the surface commissioning of NSW C, the sTGC pad trigger was tested by self-triggering (with triggers from the Pad Trigger) on cosmic muons. These tests proved useful for finding and debugging issues with the trigger firmware. The cosmic ray tests and results are described further in the next chapter.

NSW A was completed in June 2021 with NSW C commissioning ending in September 2021. The completed wheels were transported from the commissioning site to ATLAS and lowered into the cavern. NSW A was lowered into ATLAS (lowering shown in Figure 3.13) July 12th, 2021 and NSW C was lowered into the cavern November 4th, 2021. Once installed in ATLAS, the NSWs were reconnected to gas, cooling, electronics, and readout systems and the commissioning tests were repeated to ensure the NSWs were functioning as expected.

Figure 3.13: Lowering of NSW A into the ATLAS cavern, the first NSW to be installed in ATLAS. Photo courtesy of ATLAS.

The NSWs are currently part of ATLAS Run 3 data taking.

Chapter 4

Pad Efficiency Studies

As discussed in the previous chapter, the pads of the sTGCs serve a vital role in the Muon Spectrometer end-cap trigger through mechanisms referred to as logical towers. Logical towers of pads are multiple layers of pads which overlap in ϕ and R. Coincident pad hits within a logical tower form a trigger candidate, where at least three out of the four layers on both (Pivot and Confirm) wedges have hits. The towers of overlapping pads on the two wedges are combined to find an eight-layer trigger. This determines the region of strips to be read out for online track segment reconstruction. It is therefore important to develop methods of estimating the efficiency of the pads and the Pad Trigger.

This chapter will cover analyses of pad data collected during cosmic ray tests of one sTGC large sector during NSW surface commissioning, as well as data collected from the New Small Wheels after installation in ATLAS, during the Fall 2021 Pilot Beam and early in Run 3.

4.1 Experimental Setups

Data for the pad efficiency studies was collected using the Pad Trigger, which is described in further depth in Section 3.5. Pad hits (threshold-crossing signals) are digitized by the VMM and sent off-chamber to the sector's Pad Trigger (PT) board located in the NSW rim crate. In the normal operating mode, the PT finds a coincidence (pad hits in three out of four layers of each wedge within a logical tower) and signals are sent from the PT back to the front-end boards on the chamber so that the digitized strip trigger signals for the strips under the triggered logical tower are read

out and used to create track segments. For the Pad Trigger tests used in this study however, the strip readout chain was bypassed, with the pad data written to disk.

In order to estimate the pad efficiency, the pad hits need to be matched to logical towers[1] to find how frequently one layer of a logical tower fails to record a hit in coincidence with the other layers. An event is all data recorded for a given readout window surrounding a coincidence of pad hits within a logical tower found by the PT. The pad efficiency depends on both the behaviour of the pads, the energy and track angle of the charged particle passing through the detector and the proximity of the charged track to a wire in that layer. By examining the data for pad coincidences, potential errors with the Pad Trigger and pad readout system can be found in addition to quantifying the pad efficiency.

4.1.1 Surface Commissioning Cosmic Ray Tests

The Pad Trigger was implemented during the surface commissioning of NSW C to serve as a self-triggering mechanism for sTGC cosmic ray testing. While the sTGC trigger technology was developed over a period of many years, these cosmic ray tests were the first opportunity for the NSW community to test the Pad Trigger on a full working sector in the NSW. The sTGCs were only filled with CO_2 during surface commissioning as operating with the CO_2 n-pentane mixture requires a dedicated gas mixing room. The sTGCs are much less efficient when filled with only CO_2 than when filled with the working CO_2 n-pentane mixture.

Data was collected with NSW Sector C13, which is highlighted in Figure 4.1, with the sTGCs operated at a high voltage setting of 2800 V, which is the nominal high voltage for operating the sTGCs.

4.1.2 Pilot Beam Tests

NSW A was the first completed Wheel and was lowered into the ATLAS cavern during Summer 2021. NSW A was fully connected to cooling, gas, electrical, and readout systems by the fall, with trigger and readout commissioning completed in time for the pilot beam of the LHC. During the period without stable beams, data was collected by self-triggering from cosmic rays with one large sector (A15) operating at

[1]Each pad typically belongs to four unique four-layer logical towers.

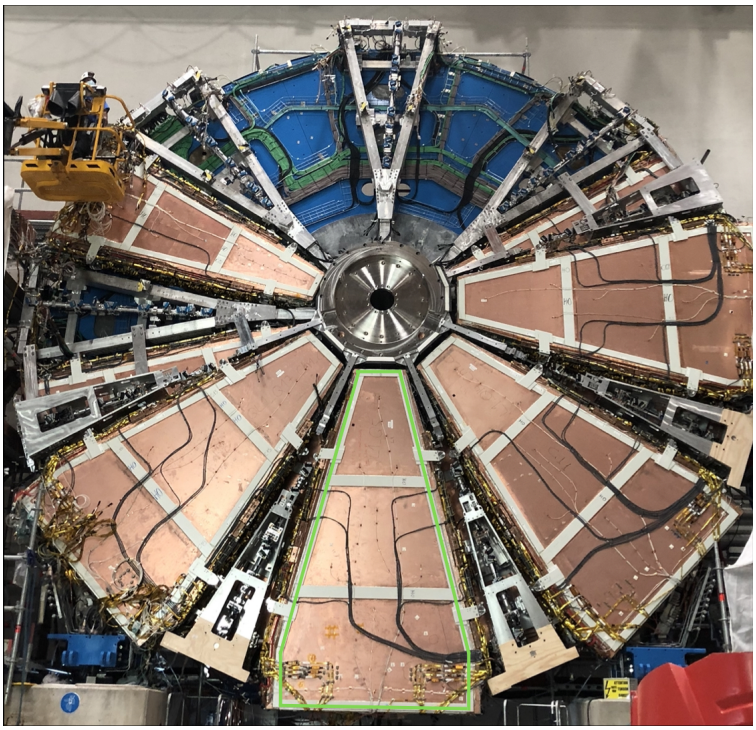

Figure 4.1: Picture of NSW C taken during Summer 2021 surface commissioning. Sector C13, marked by the green border, was used for taking self-triggering cosmic ray data.

a reduced voltage of 2500 V[2]. During the LHC Pilot Beam (10/18/2021-10/30/2021), self-triggering pad data was collected from two sectors, the large sector A15 and the small sector A10. The chambers were filled with the CO_2 n-pentane gas mixture and were operated at the nominal high voltage setting of 2800 V. The data was collected during periods of stable beams as well as during beam splashes, where the beam is wide and strikes a collimator, producing large horizontal showers of particles within the experiment that can be observed in every sub-system.

4.1.3 Run 3 Standalone Tests

During the start of Run 3, NSW C was used for trigger testing. The sTGC trigger team conducted simultaneous data runs on C15 (a large sector) and C16 (a small sector) from 13.6 TeV collisions by self-triggering (utilizing the Pad Trigger). Other runs utilized the ATLAS Level 1 (L1) trigger as an external trigger and read out

[2]The standard data-taking safety procedure within the Muon Spectrometer is to operate the various subsystems at lower high voltage settings until stable beams are declared.

all pad hits within a set time frame after each muon trigger. During a four week period of no beam due to the failure of a cooling tower controller, cosmic ray data was collected for every sector of NSW C by self-triggering.

4.2 Cosmic Rays

There are a number of known astronomical phenomena outside of the solar system that produce radiation of long-lived particles, such as protons, alpha particles, and heavy nuclei. This radiation, in addition to particles from solar flares, constitutes the bulk of cosmic rays. The particles interact strongly and electromagnetically with nuclei in the atmosphere and produce showers of particles, or secondary cosmic rays. Depending on the initial interaction of the primary cosmic ray particle, the secondary cosmic rays can consist of photons, electrons, pions, muons, and/or neutrinos. The production of secondary cosmic rays and the typical track lengths of the products are shown in Figure 4.2. Most of the secondary cosmic rays are short lived and do not reach the surface. However as muons have a mean lifetime of 2.2×10^{-6} s [21], they are more likely to be detected at sea-level[3], and so comprise a large fraction of cosmic radiation that is detectable by the sTGCs[4]. As cosmic radiation originates outside the atmosphere, primary cosmic rays are impacted by factors such as geomagnetism and solar effects (plasma and solar wind). For the purpose of this study, these effects on the distribution of initial and secondary cosmic rays can be neglected. If production of cosmic muons is uniformly distributed in angle, the angular distribution of detected cosmic muons at the surface is heavily dependent on the angle from zenith, with the distribution of cosmic muons varying with respect to the zenith angle θ as $\cos^2\theta$ [14]. Larger deviations from the vertical correspond to longer track lengths (more material to lose energy via ionization and greater opportunity for decay).

During production and assembly, many sTGC modules were tested with cosmic rays. In these tests, the module was typically held horizontally with a pair of scintillators located above and below the module so the signals read out were from cosmic rays that passed every layer of the module [23]. The horizontal orientation of the

[3]Cosmic muons have speeds greater than 90% the speed of light. From special relativity, the path length (10 km from the top of the atmosphere) is contracted.

[4]Neutrinos are also long lived and likely to reach the surface, but are practically invisible to the sTGCs as they are neutral and have a very small interaction cross-section. Electrons and positrons produced from cosmic rays are able to be detected at the surface, but have a lower flux and tend to have lower energies than muons [14].

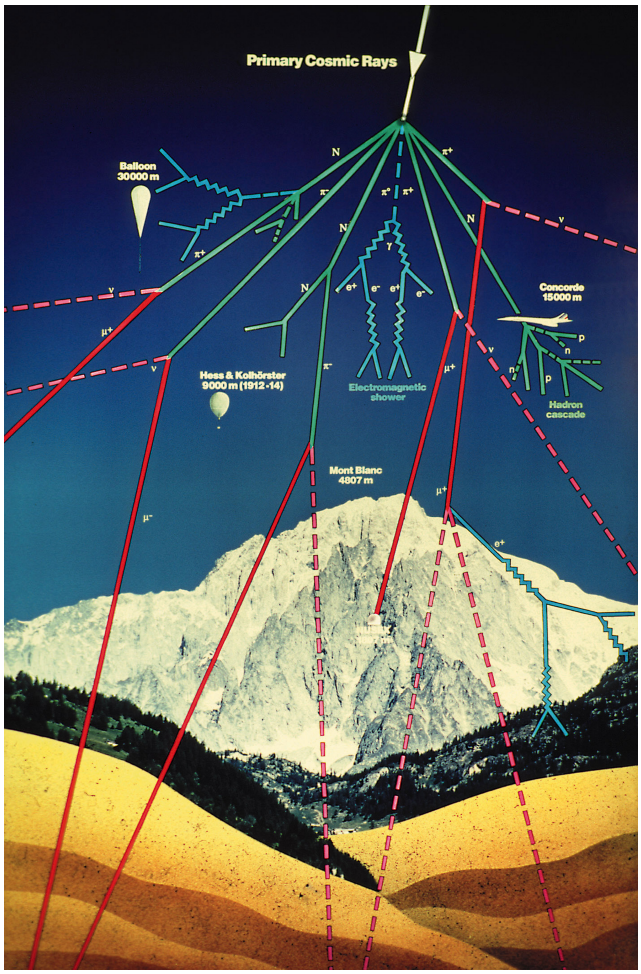

Figure 4.2: Illustration of primary cosmic ray and production of cosmic shower [22]. The production of muons is shown, along with the muon tracks penetrating the surface.

tested modules and the use of scintillators allowed for detecting the highest rate of cosmic muons.

The logical pad towers were designed to select tracks originating from the Interaction Point with each logical tower having a limited opening angle. The pairs of four-layer logical towers are staggered between the Pivot and Confirm wedges to ensure only a narrow range of track angles will trigger a given band of strips. This staggering results in a very small angular acceptance for an eight-layer logical tower, compared to a four-layer pattern which has an an acceptance of approximately 100 degrees. This is described further in Appendix A.1. Tracks originating at the IP are much closer to orthogonal to the surface of the NSW than the majority of cosmic muons. Thus, even for the four-layer patterns, the NSW detection rate of cosmic rays

is low. The looser 3 out of 4 layer trigger requirements were used in the cosmic ray tests to allow the sTGC to trigger on the greatest possible number of cosmic muons.

The rate of cosmic rays detected is proportional to the size of the detector, resulting in the largest pads in the NSW in the QL2 and QL3 modules detecting the largest number of cosmic rays[5].

4.3 Finding Pad Hit Coincidences

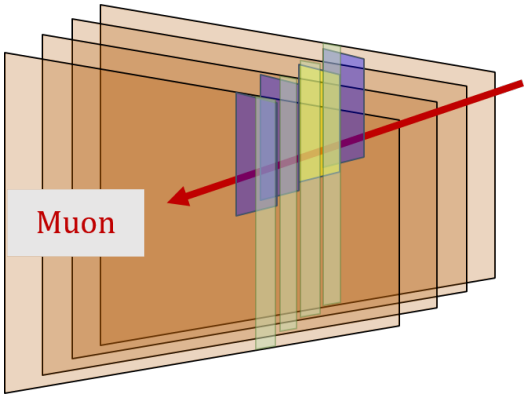

Figure 4.3: Diagram of a muon track traversing four layers of sTGC. The pad hits determine a region of strips to be read out. Figure courtesy of Siyuan Sun.

A single logical tower is formed from eight pads chosen so that an IP-pointing track could produce hits in all eight layers of sTGC pads. A logical tower can be broken down into a set of four pads (that overlap in R and ϕ) on each wedge. The pad trigger matches four-layer logical towers that have three or fours hit in coincidence to corresponding four-layer logical towers with hits in coincidence on the other wedge in the sector. An example of a muon track producing hits in a four-layer logical tower is shown in Figure 4.3. For the cosmic ray tests during surface commissioning, the Pad Trigger was triggered on these four-layer logical towers, so that any coincidence of three or four pad hits within one of these four-layer patterns would trigger the read out of all of the pad channels in the sector. For the Pilot Beam and Run 3 self-triggering tests, a sector was read out following a three-out-of-four and three-out-of-four coincidence within a full eight-layer logical tower.

Almost every pad is part of four separate four-layer logical towers which segment

[5]Within ATLAS, the pads nearest the beam (in the QS1 and QL1 modules) would detect the highest rate of muons as the rate is approximately constant in $|\Delta\eta|$.

the physical pad into four logical pads. The border of a logical pad is defined by the overlapping area of the pads with the four-layer logical tower. A map of the logical pads on one layer of a Large sector is shown in Figure 4.4. The lower radius pads are disconnected from the trigger and do not contain any logical towers. This region is not covered by the Big Wheel and there are no muon triggers to veto for $|\eta|> 2.4$.

Events are defined, in this context, as all pad hits from the tested sector within a given time window surrounding a coincidence found by the PT. As described in Chapter 2, the Bunch Crossing (BC) clock has a 40 MHz frequency and is one of the most important clocks in ATLAS, and each Bunch Crossing ID (BCID) is 25 ns (1/40 MHz) wide. During the surface testing runs of C13, 5 BCIDs were read out, with the trigger-causing hits centred (in time) in the readout window.

In this study, only the four-layer logical towers were considered and the set of pads that form the logical tower are referred to as a pad pattern. The pattern matching algorithm went through each event in a given data file and sorted the pad hits by quad and layer. To avoid bias in the pattern selection, the list of four-layer logical towers was randomized for each event and then looped through to find patterns that contain hits within the event. If at least three layers of the pattern were hit then two logs were updated: the pattern occurrence log which keeps track of how many times any given pattern was found to have three or four layers with hits and another log that kept track of how those hits are distributed per layer. The two logs provide information on the number of times a given layer was missed when the other layers had hits.

Timing constraints were imposed by requiring that any in-coincidence pad hits that form a logical tower have BCIDs within a set range of each other. BCID is a counter that increases every 25 ns over the course of a run. When a trigger is found, the readout window is centred around the BCIDs associated with the hits that initiated the trigger. If the readout window is 8 BCIDs wide, the triggering hits would be assigned to relative BCIDs (relBCIDs) 3 or 4, with the earliest and latest hits captured by the readout window having relBCIDs of 0 and 7 respectively. Examples of 8 relBCID readout windows are shown in Figure 4.5.

Given a set of pad hits that lie within a logical tower, the corresponding relBCIDS are first considered. A relBCID that has at least two hits is selected as the primary relBCID for the coincidence. Then if there were hits within one BCID of the primary relBCID, those hits would also be accepted as part of the coincidence. Examples of hits spread in time are shown in Figure 4.5 with two cases of timing that would be

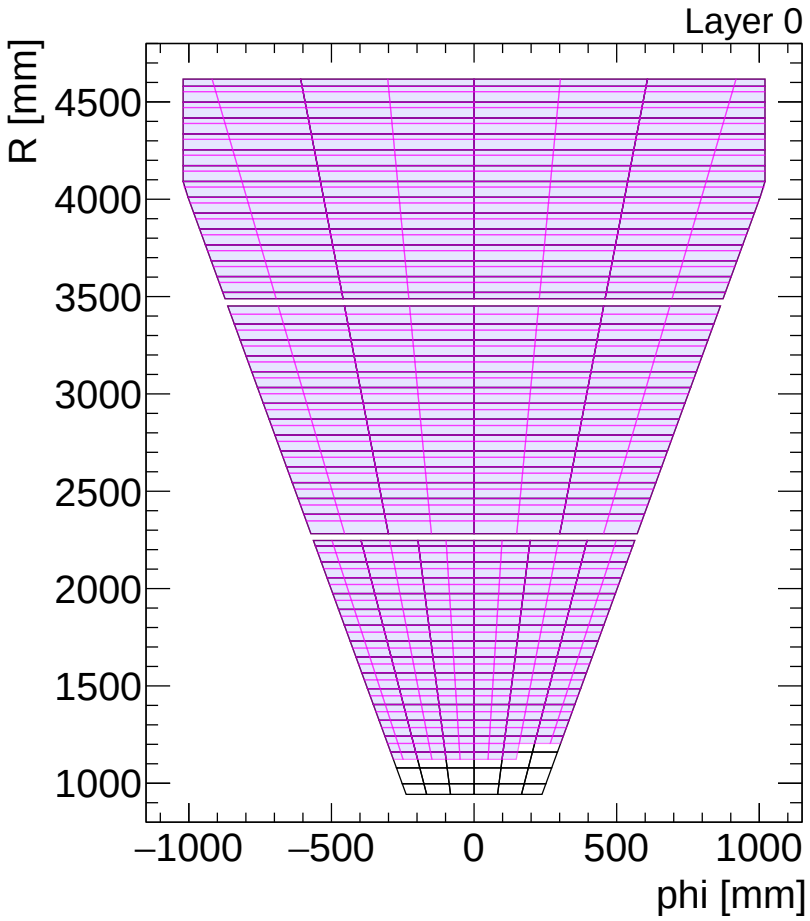

Figure 4.4: The logical pads (pink borders and blue fill) formed from four-layer logical towers in the Pivot (first four sTGC layers of a large sector, counting from the IP) projected onto the physical pad outlines (black borders) for the first large Pivot layer. Almost every physical pad belongs to four separate four-layer logical towers.

accepted as a coincidence. This method allows for pad coincidences to be spread over a maximum of 3 BCIDs.

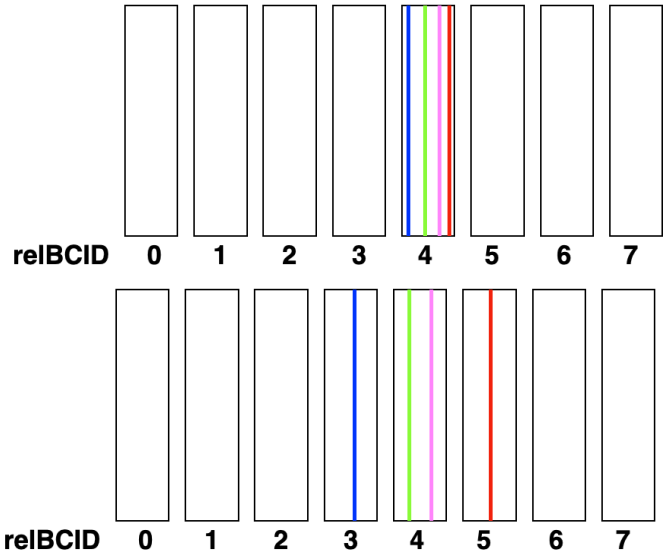

Figure 4.5: Examples of hits on four layers over an 8 relative BCID (relBCID) readout window, where each layer in a logical tower is designated by a different coloured line. In the first example (top), all four hits occurred within the same relBCID. The second example (bottom) shows hits spread in time. As two hits occurred in relBCID 4, that would be selected as the primary BCID for a pattern. Then as the hits at relBCIDs 3 and 5 are within one BCID of the primary, those hits would also be accepted as in coincidence.

4.4 Pad Efficiency Calculation

After applying the pattern matching algorithm to the data, all pad hits in coincidence have been assigned to the corresponding patterns. The number of times a given four-layer pattern had hits in coincidence and the per-layer distribution of hits within that pattern were logged. Using these hit logs, one can find which pads were geometrically missed in a track (from extreme angles of cosmic rays or particles that were stopped in the detector) or did not register hits after a charged particle passed through them (the "true" efficiency of the pads).

The efficiency formula for a logical pad follows from considering the probability that a specific pad was hit, given that the three other layers in a pattern that contains that pad were also hit. Bayes' Theorem, given as Equation 4.1, is used to derive an expression for pad efficiency.

$$P(A|B) = \frac{P(B|A)P(A)}{P(B)} \tag{4.1}$$

The probability of a hit on the pad under consideration, $P(p)$, is proportional to the hit rate on the pad, which can be calculated knowing the number of events (defined in Section 4.3 as pad hits read out within a range of BCIDs surrounding a trigger) in which the pad was hit, n_p, and the total number of events with any trigger, n_T as

$$P(p) = \frac{n_p}{n_T}. \tag{4.2}$$

Let n_4 be the number of events where all four pads in the pattern were hit. Let n_3 be the number of events where the pad was not hit when the other 3 layers of the pattern were hit. The probability that the three other layers in the pattern were hit is given by $P(3)$ which is

$$P(3) = \frac{\text{events where the other 3 layers in a pattern were hit}}{\text{total number of events}} = \frac{n_4 + n_3}{n_T}. \tag{4.3}$$

The probability that the other 3 pads in the pattern were hit given a hit on the reference pad is

$$P(3|p) = \frac{n_4}{n_p},\ n_p > 0. \tag{4.4}$$

Then it follows from Bayes' rule that

$$P(p|3) = \frac{P(3|p)P(p)}{P(3)} = \frac{n_4}{n_p}\frac{n_p}{n_T}\frac{n_T}{n_4 + n_3} = \frac{n_4}{n_4 + n_3} = e_{lt}. \tag{4.5}$$

This is the formula for calculating the efficiency of a reference pad within a single logical tower, e_{lt}.

4.5 Findings from Surface Cosmic Ray Tests

As the majority of cosmic rays do not have an angle of incidence consistent with a muon originating at the IP of ATLAS, using the full 8-layer logical towers as a trigger would greatly restrict the angle of acceptance and thus the trigger rate for cosmic ray tests. Runs conducted with the three-out-four and three-out-of-four coincidence requirement would require weeks or months of data collection in order to record enough events for analysis to be conducted. With the NSW commissioning schedule, it was not possible for cosmic runs to be conducted with such a strict constraint on the Pad Trigger. Instead, the two wedges in the sector were triggered independently

so the wedges would be read out if concurrent hits within a logical tower were found on one wedge. With the individual four-layer patterns having much larger angular acceptances than the full logical towers, this allowed for much shorter data collection periods.

With the limited statistics from cosmic rays as well as operating with only CO_2 (which was expected to lower the efficiency) filling the chambers, the data collected from the surface cosmic ray tests do not allow a definitive assessment of the efficiency of the NSW trigger. However, the data collection process exposed issues with the trigger firmware and allowed for optimization of the trigger latency. Over the course of commissioning and cosmic ray tests, the trigger firmware was modified to correct issues that came to light via the tests. As a result, direct comparisons between runs are difficult to make, as the trigger setups were varied.

The per-pad distribution of hits on the Confirm wedge of the tested sector for a cosmic ray test run that was analyzed is shown in Figure 4.6. The rate of hits on individual pads scales with the area of the pads, where the largest pads received proportionally more hits than the smallest pads. If the opposite result was observed, for example if the narrowest column of pads received more hits than the widest, it would indicate that mapping of readout channels to physical pads was reversed. The maps of pad hit distribution (heat maps) have been useful for debugging similar issues.

The pad hit data was then used to calculate logical pad efficiency. The efficiencies of the logical pads on two layers of the Confirm wedge are shown in Figure 4.7. While there are no clear trends as a function of layer depth, it is clear that the pads on Layer 5 had a higher efficiency than those on Layer 4.

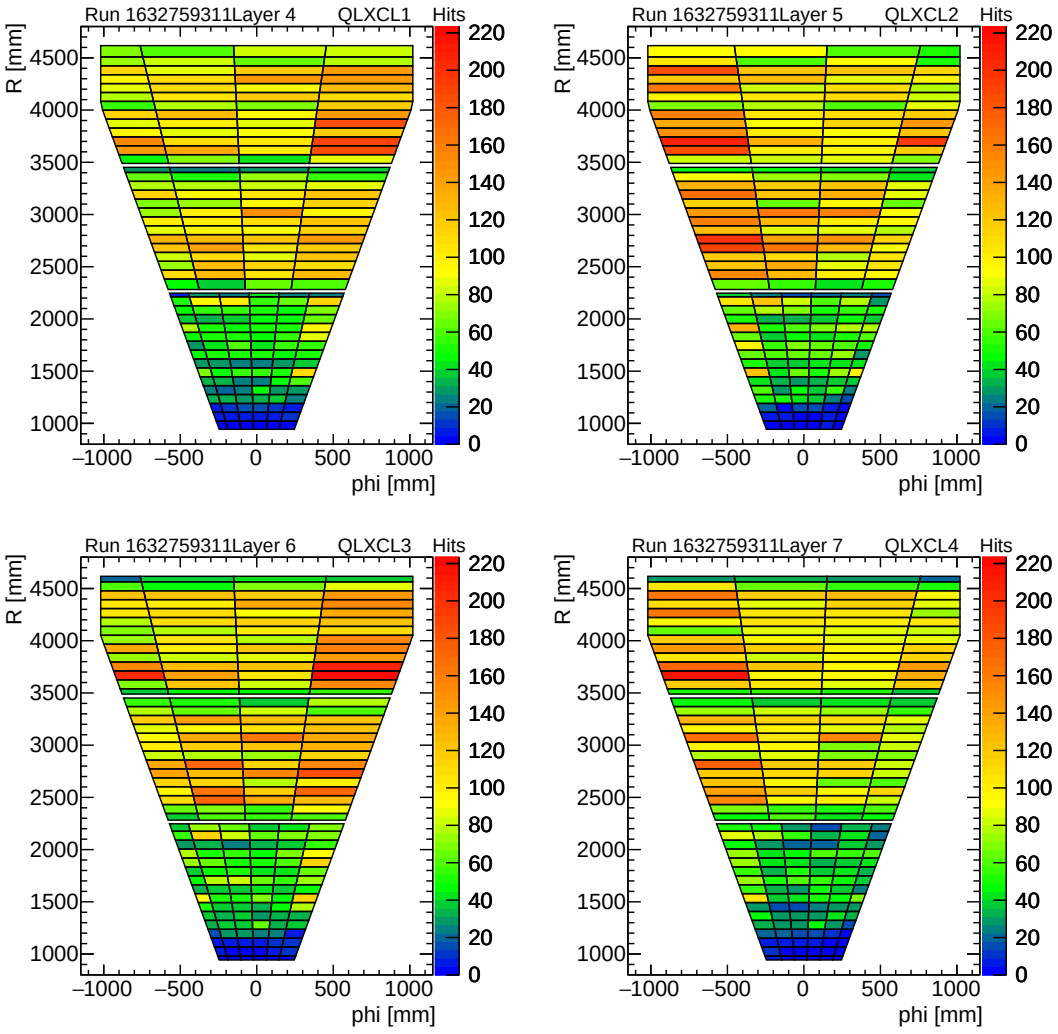

Figure 4.6: Distribution of cosmic ray hits on the Confirm wedge of C13 from one run collected with self-triggering on pad hits. The pad staggering can be observed: layers 4 and 5 are identical but one is inverted (around the vertical) with respect to the other; the same is true for layers 6 and 7. The pads of layers 6 and 7 are offset vertically by half a pad-height with respect to the pads of layers 4 and 5.

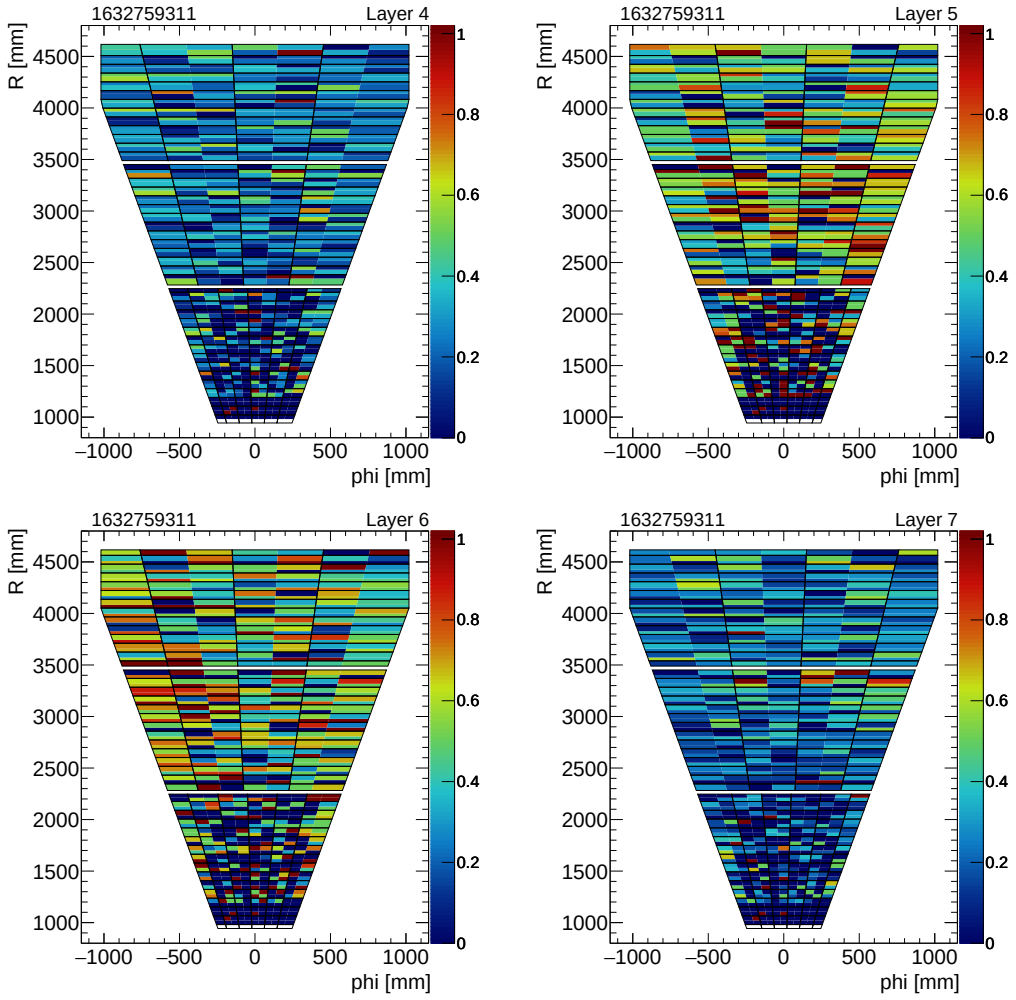

Figure 4.7: Map of logical tower efficiency for C13 during surface cosmic ray tests for two layers on the Confirm wedge. The inner layers (layers 5 and 6) of the wedge have a much higher efficiency than the outer layers (layers 4 and 7).

4.6 Findings from Pilot Beam

With the hard work of the sTGC and MM commissioning teams, NSW A was operational for the October 2021 pilot beam. The readout and trigger teams were able to collect data from two sectors (a large and a small sector) on the wheel during stand-alone runs. The distribution of pad hits on the large sector A15 is shown in Figure 4.8. The difference in hit distribution between the cosmic ray tests and the beam data is notable, with the pads lower in R (closer to the beam) receiving the most hits during the beam runs.

The efficiency maps for two layers are shown in Figure 4.9. The efficiencies were much higher compared to the efficiency maps in Figure 4.7. This was a result of triggering on particles originating from proton beam interactions as well as operating with the CO_2 n-pentane mixture, as opposed to only CO_2. The wire planes have internal supports within the modules that run parallel to the strips. In Figure 4.9, the bands of inefficiencies due to the wire supports are visible on the QL1C logical towers.

A histogram was filled with the efficiency values given in Figure 4.10. If all pads that are connected to the trigger were functioning, the larger pads in the innermost region (QL1) should have registered at least one hit. However, as can be seen on Layers 1 and 3 in Figure 4.8, there are pads with no hits adjacent to pads with relatively large numbers of hits. Every logical pad within a pattern that contained a pad that received no hits would have a 0% efficiency, regardless of how many hits in coincidence the other three pads registered. As these 'dead' pads are not indicative of the typical functionality of most pads, logical towers that contained a pad that did not receive any hits were excluded from the efficiency calculation.

The logical pad efficiency histogram demonstrates that many logical pads recorded only four-out-of-four hits in coincidence during the run and were calculated to be 100% efficient, which could occur if only a few muons passed through that logical tower. The mean efficiency of the logical pads is about 75% and approximately 74% of the pads that are connected to the pad trigger contained a logical pad with an efficiency greater than 90%.

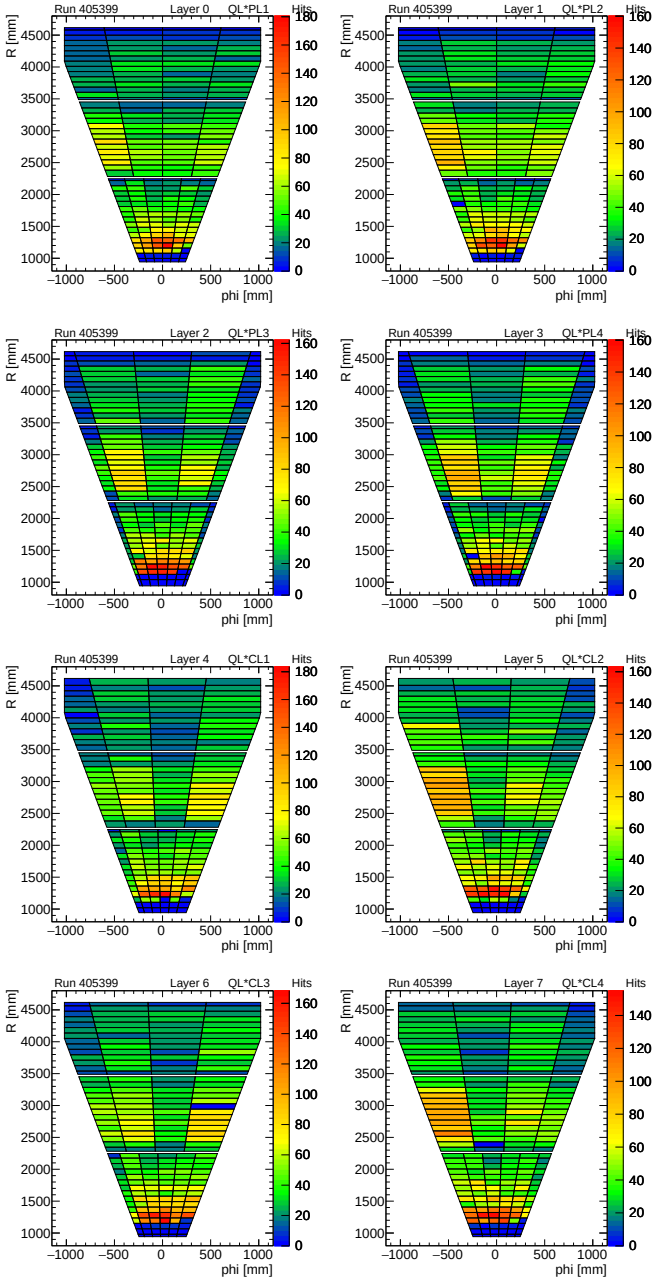

Figure 4.8: Distribution of pad hits on A15 during a pilot beam run. Data was recorded via self-triggering, with the trigger requiring 3/4 coincidences on both wedges. There are no logical towers or trigger channels on the inner (low R) end of the QL1 modules, so those pads are not expected to have any hits.

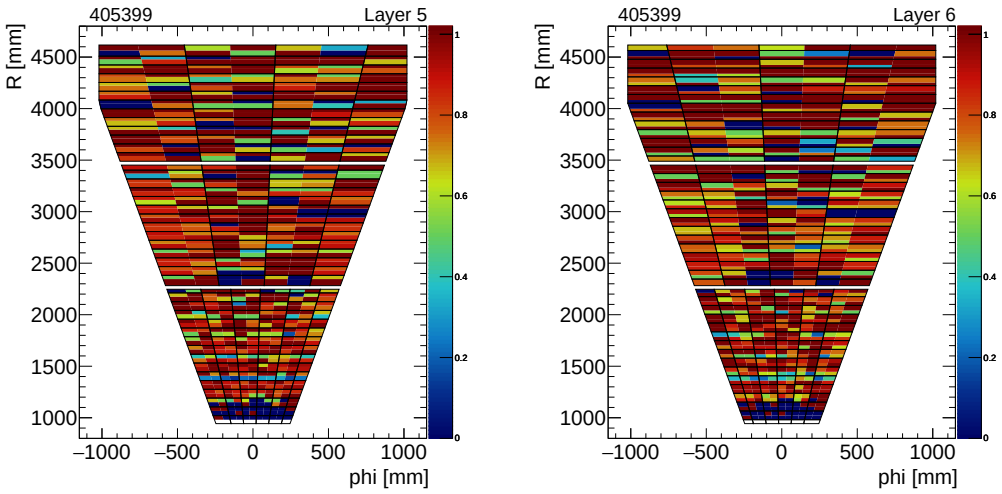

Figure 4.9: Map of logical pad efficiency for two layers of A15 calculated from the data in the run shown in the hit maps in Figure 4.8. Bands of inefficient logical pads can be seen on the logical towers of QL1C, at approximate R values of 1300 mm and 1600 mm on Layer 5 (left) and 1400 mm on Layer 6 (right).

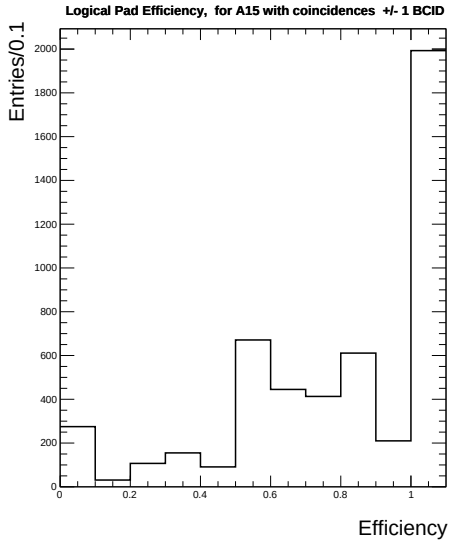

Figure 4.10: Histogram of logical pad efficiency for A15 during the pilot beam. Logical towers that contained a pad with no hits were excluded from the efficiency calculation. The final bin corresponds to logical pads with efficiencies equal to 1. While many logical pads were calculated to have an efficiency of 100%, those pads likely received relatively few hits.

4.7 Preliminary Findings from Run 3

When the distributions of pad hits from self-triggering runs with proton-proton collisions (p-p) on C15 and C16 (Figures 4.11 and 4.12 respectively) were combined with observations of on-line data, it became clear to sTGC experts that two VMMs of the Q2 modules were deactivated for every sector in the NSW. Observing the effect in two separate (self-triggering pads and online data acquisition) systems indicated that the issue was occurring with the configuration files. The configuration files used for data collection and operations had masked those VMMs[6], so no data was read out in those regions. This error was corrected in time for the ATLAS alignment runs, where the toroid magnets were turned off and the NSW and Big Wheels measured straight muon tracks.

The masked VMMs on layers 0 and 1 of C15 and C16 resulted in large regions of pads that were disconnected from the trigger. Lack of high voltage on QL3CL1 and QL1CL4 of C15 and QS1PL4 of C16, and noise issues on QL2CL2, also resulted in entire quadruplets with no four-out-of-four coincidences. As described in Section 4.6, the logical towers in those regions were excluded from the efficiency calculations. As seen in Figures 4.13 and 4.14, there were large 'dead' regions with 0% efficiency. The histograms for logical pad efficiency for C15 and C16 are shown in Figure 4.15, where 'dead' regions were excluded from the efficiency calculation. The mean logical pad efficiency for C15 is about 71% and for C16 is about 77%. A smaller percentage of trigger-connected pads were calculated to be highly efficient in comparison to the pilot beam test, with approximately 62% of the pads on C15 and and 50% of the pads on C16 within the region where all four layers could register hits containing at least one logical pad with an efficiency greater than 90%. Most of the pads were efficient with about 79% and 83% of the trigger-connected pads on C15 and C16, respectively, containing at least one logical pad with an efficiency greater than 75%.

[6]This was the result of a cut-and-paste error where the configurations for the first two commissioned sectors, which at the time needed to have those VMMs masked, were applied to all sectors.

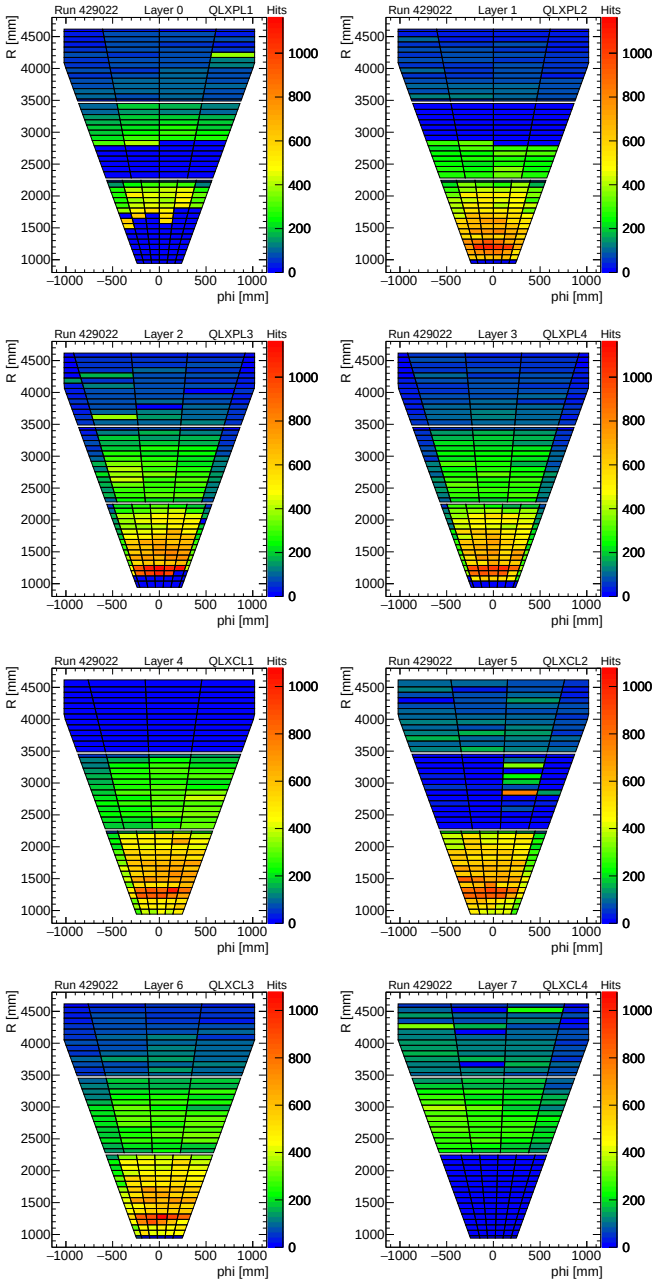

Figure 4.11: Distribution of pad hits on C15 during a self-triggering run with 13.6 TeV collisions. On QL2PL1 and QL2CL2 (approximately 2200 mm to 3500 mm in R), large pad regions with no hits can be seen, due to masked VMMs in the configuration files as well as a lack of high voltage on QL3CL1. The two quadruplet layers with no hits (QL3CL1 and QL1CL4) lacked high voltage. The few pads with hits on QL2CL2 were the product of a noise issue.

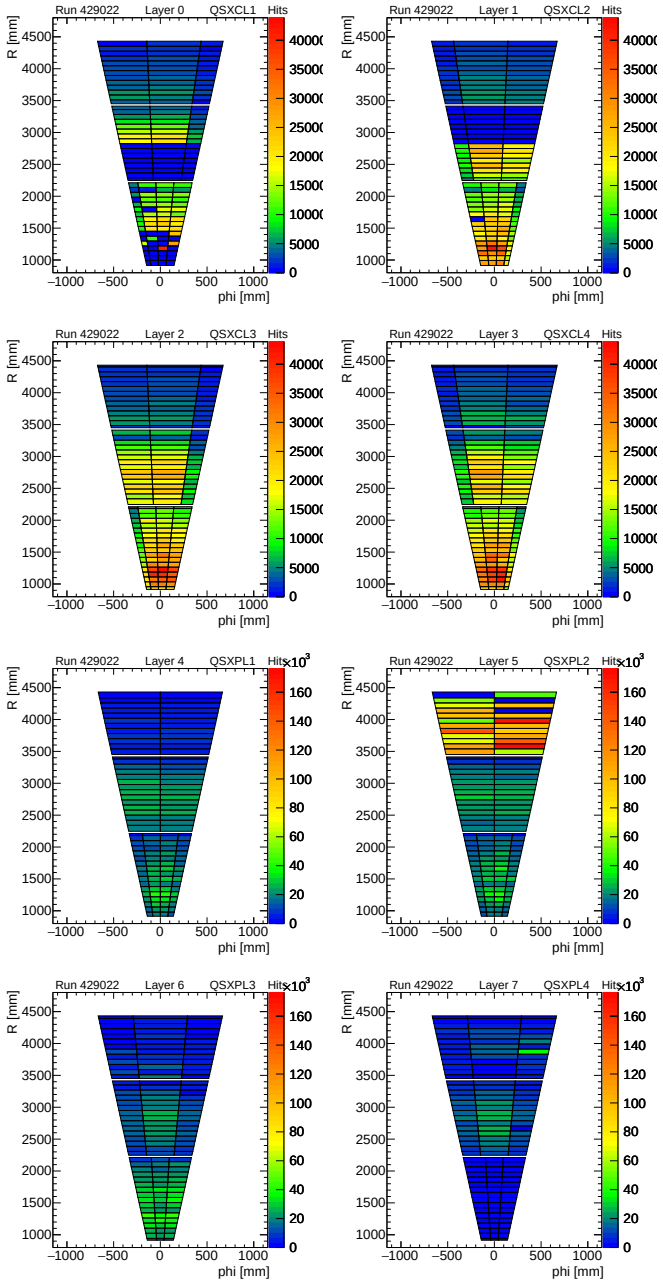

Figure 4.12: Distribution of pad hits on C16 during a self-triggering run with 13.6 TeV collisions. On QS2CL1 and QS2CL2, large pad regions with no hits can be seen, due to masked VMMs in the configuration files. QS3PL2 had a noise issue that resulted in a surplus of 'hits' on that quadruplet layer with respect to the other layers of QS3P.

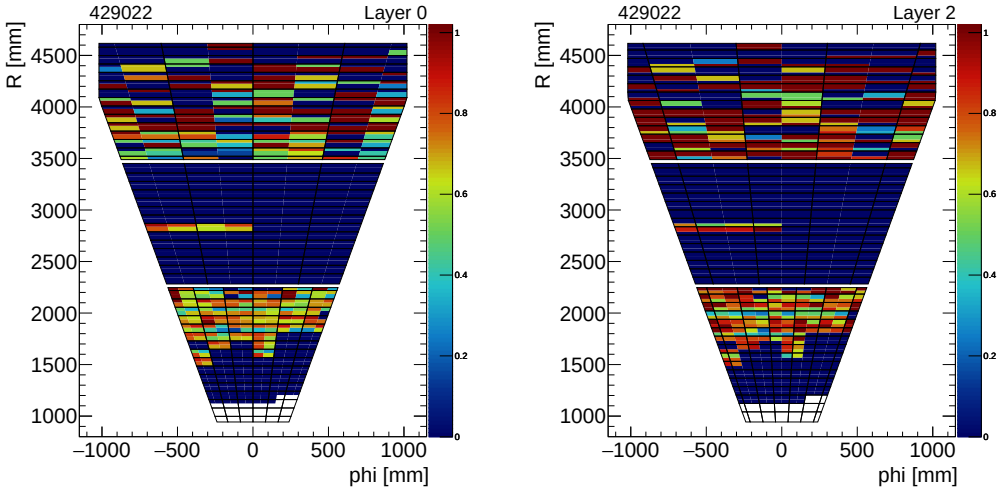

Figure 4.13: Map of logical pad efficiency for two layers of C15 calculated from the data in the run shown in the heat maps 4.11. Bands of inefficient logical pads can be seen on QL1P, at approximate R values of 1700 mm and 2000 mm on Layer 2 (right). The inefficient regions (most of QL2P and the inner apart of QL1P) are due the VMM and HV problems shown in Figure 4.11.

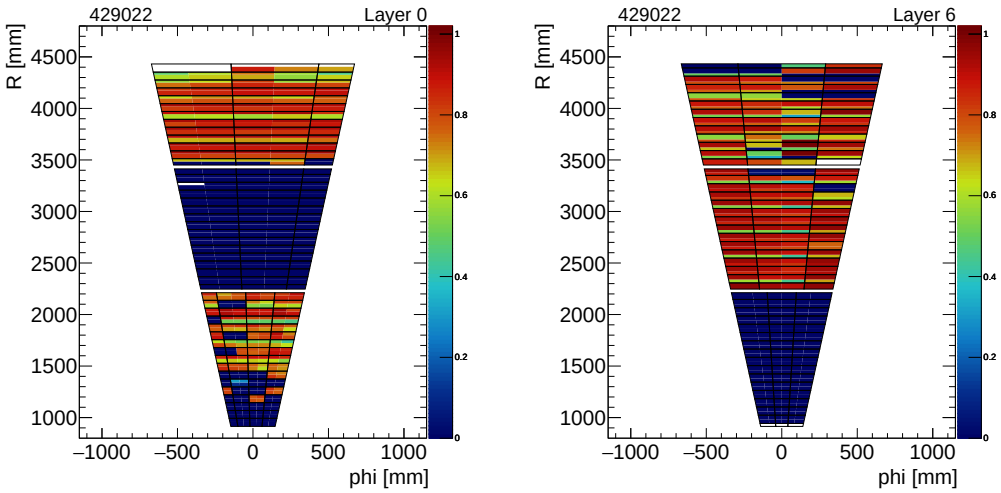

Figure 4.14: Map of logical pad efficiency for two layers of C16 calculated from the data in the run shown in the heat maps 4.12. Bands of inefficient logical pads due to wire supports can be seen at approximate R values of 1500, 1700, 1900, 2100, 3500, 3700, 3900, and 4100 mm on Layer 0 (left) and at 2300, 2600, 2800, 3100, 3300, 3500, 3600, and 4000 mm on Layer 6 (right).

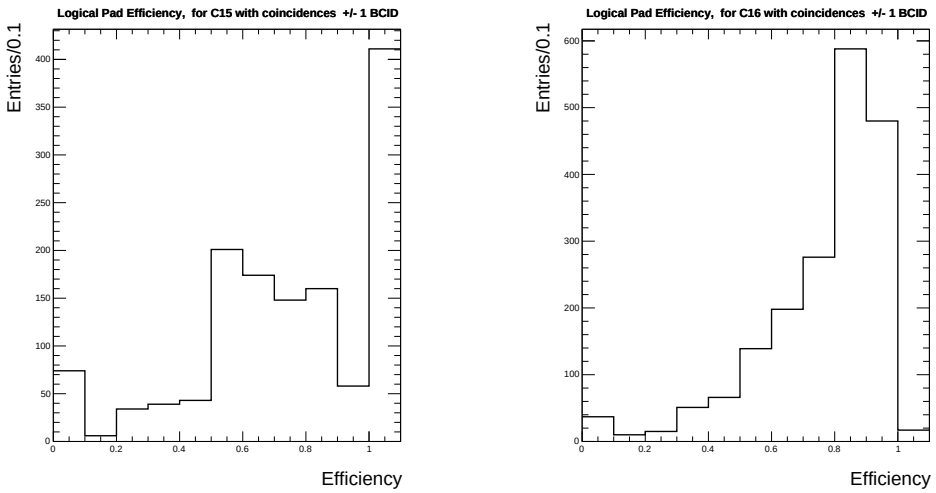

Figure 4.15: Histograms of logical pad efficiency for C15 (left) and C16 (right) during a p-p run. Logical towers that contained pads with no hits were excluded from the efficiency calculation.

4.8 Sources of Inefficiency

While most logical towers are very efficient, there are multiple sources of pad trigger inefficiency. On an individual pad basis, if a pad is shorted to its neighbour or is extremely noisy, then ionization electrons produce avalanches on the wires but the pad will not detect the induced signal. However, there are also issues that affect entire layers or rows of logical towers.

As discussed in Section 3.4, a muon that passes between two wires will ionize electrons in a region of low electric field. The ionization electrons have a long drift time, resulting in a delayed signal in comparison to the typical response time. This inefficiency in timing is mitigated by staggering the wires between layers, which reduces the likelihood of a muon passing exactly between two wires on more than one of the four layers. As the NSW trigger only requires three out of four layers to have hits in coincidence, tracks that do produce delayed signals on one layer can still be accepted as trigger candidates.

Three-layer logical towers have a wider angular acceptance than the four layer logical towers, so tracks with relatively extreme angles may pass through only three layers of a logical tower. As such, it is consistent that the pads are much less efficient at triggering on cosmic rays than muons originating from the IP. The angular acceptance difference between three and four layers could explain the lower efficiencies observed for the first and last layers compared to the second and third. As during data taking in ATLAS, the Pad Trigger requires three-out-of-four and three-out-of-four, the rate of triggers from the cosmic ray background is negligible.

In the pad efficiency studies, we assumed that every layer was capable of registering hits. However, if one layer lacks high voltage, such as QL3CL1 of C15 (Figure 4.11), or contains VMMs that do not read out data, like QL2CL1 and QL2CL2 of C15, this would not be the case. As the first layer of QL3C of C15 was not recording any pad hits, it ensured that there were no possible 4 out of 4 patterns in that quadruplet. Thus, the pads on QL3C of C15 would be assigned efficiencies of 0% by the definition used in this analysis, which is not reflective of the true functionality of those pads. In the event that this issue cannot be fixed, the pads on a missing layer would be assigned 100% efficiency and the logical towers to which they belong would require hits on two out of the three remaining layers to form part of a trigger.

The wire supports are solid insulators glued to the cathode boards, with gaps in the graphite layer where the supports are located (see Section 3.4). The heights of the

wire supports are the same as the height of the gas gap, which reduces the effective size of the gas volume in that region to zero. The break in the graphite coating results in no electric field in the area around the supports. The inefficiency and reduced hit rate of the strips in the region of the wire supports were observed at all stages of sTGC testing. The radial position of the wire supports is staggered between layers to reduce the overall impact of the lowered efficiency.

The trigger requirement (three-out-of-four and three-out-of-four) allows for some layers to be less efficient while still producing fast trigger segments that accept muon tracks that point toward the IP and reject background.

Chapter 5

NSW GIF++ Test Beam

NSW test beam data collection took place from October 20th to November 2nd, and November 10th to November 14th 2021. During the data collection period, the sTGC test beam team had 24-hour shift coverage. The motivation for the test beam was to measure the sTGC detector performance in a high background environment. The predicted maximum background that the NSW will observe during the HL-LHC is up to 15 kHz/cm^2 for the innermost regions. The CERN Gamma Irradiation Facility is able to provide a similar high-background environment.

5.1 Gamma Irradiation Facility

The Gamma Irradiation Facility (GIF++) is located on a beam line[1] that can supply muons with momentum up to 100 GeV/c, produced from the SPS H4 beam line in the CERN North Area[2] and contains a cesium-137 (^{137}Cs) source that produces a high-rate gamma field. This allows for GIF++ to replicate the expected background conditions of the HL-LHC. The LHC experiments are able to test hardware upgrades for HL-LHC and study how they will function under the high background environment of HL-LHC.

The gamma source is located in the centre of the GIF bunker, as shown in Figure 5.1, within a storage and raising mechanism that creates two wide radiation fields

[1]The H4 beam line was designed to deliver secondary and tertiary beams of various particle types (hadrons, electrons, muons, or ions) or an attenuated primary proton beam [24]. The muon beam for GIF++ is produced from a secondary pion beam. The conversion process can be bypassed with the pion beam sent directly to GIF++ and the upstream experiments.

[2]The North Area and GIF++ are included in the diagram of the CERN Accelerator Complex (Fig. 2.1).

(the upstream and downstream γ-fields in Figure 5.1). The rate of gamma radiation in the two fields is modulated by raising shielding plates (attenuators) on either side of the source, absorbing a fraction of gamma-rays and reducing the gamma rate proportionally to the thickness of the attenuators, allowing for the two fields to have different gamma rates [25]. The raising and lowering of the source from its storage position as well as the strength of attenuation for the two radiation fields are controlled by users in the GIF++ control room.

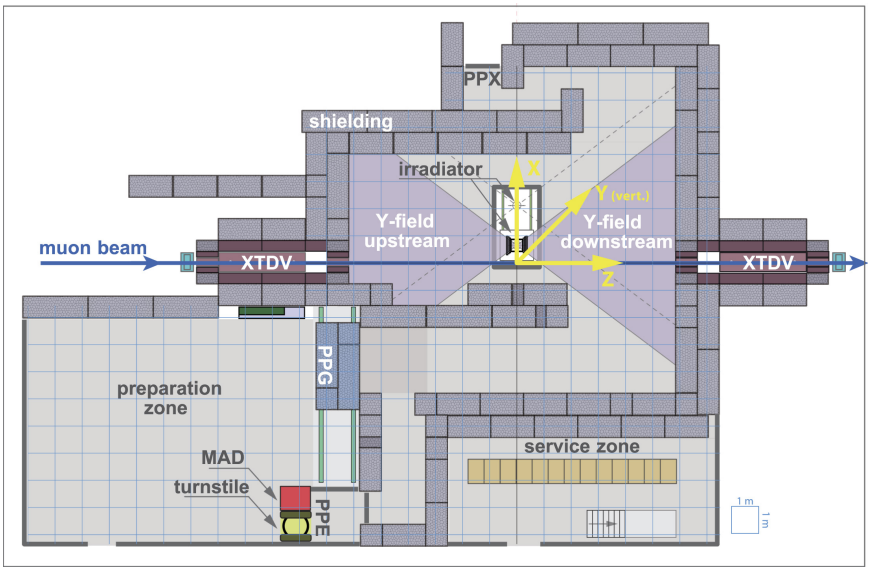

Figure 5.1: Layout of GIF++ bunker and surrounding services [26]. The NSW test beam setup was located in the downstream γ-field and the sTGC scintillators were mounted on the downstream wall, inside the bunker and in line with the muon beam. The controls for the the sTGC and MM gas and cooling systems were located in the service zone. The sTGC FELIX and triggering system were located in the preparation zone.

5.2 NSW Test Beam Setup

The NSW setup within the GIF bunker consisted of one sTGC quadruplet (a QL1C module) and one MicroMegas module with the MM located closer to the gamma source, as shown in Figure 5.2. The sTGC quad was held on a support frame that could tilt the quad[3] to a maximum angle of 20 degrees from the vertical. The sTGCs were designed for track angles of approximately 7 degrees to 31 degrees. The 20 degree

[3]The tilting mechanism was operated manually, so the angle of the support frame could only be changed when the gamma source was lowered to the 'storage' position.

tilt is near the maximum expected track angles the QL1C will observe. The sTGC module was circulated with the CO_2 n-pentane mixture (55:45) that the sTGCs use within ATLAS.

The NSW test beam experiments were set up in the downstream region of the GIF bunker (the side of the bunker where the beam exits). The maximum gamma rate incident on the sTGC module was 13 kHz/cm^2, which corresponds to an attenuation factor of 1 (no attenuators). The higher the attenuation factor a, the lower the background, with the resultant rate on the module equal to $13/a$ kHz/cm^2.

Figure 5.2: sTGC and MM test beam modules within the GIF++ bunker. Picture courtesy of Ksenia Solovieva.

The full sTGC readout chain as described in Section 3.5 was not used for the test beam. Instead, a simplified version of the readout system was used, consisting of on-detector electronics (final version of strip and pad FEBs and on-detector L1DDCs) as well as off-detector L1DDC, FELIX, and swROD, as depicted in Figure 5.3. The signals from the detector were digitized and transmitted via optical fibres to the FELIX machine located in the preparation area outside the bunker. The TDS and Pad Trigger were not utilized in the test beam readout setup.

Without the full readout system, the sTGC self-triggering mechanism could not

be used. The external triggers for the sTGC readout came from the GIF 40x40 cm^2 scintillators outside the bunker that trigger on the muon beam. In addition, the sTGC team placed a pair of 4x15 cm^2 scintillator paddles, the "sTGC scintillators", inside the bunker (in the downstream region, with a few cm separation) to trigger on a small 2x5 cm^2 overlap region. The region of coincidence was positioned so that it was located over one logical tower of sTGC pads. The sTGC could be triggered by coincidences from the GIF scintillators, the sTGC scintillators, or all 4 scintillators combined, giving a range of muon tracks (larger spread or more focused onto a single pad). The Level-1 Accept was generated by a trigger interface module with input from the scintillators. Following a L1A, any sTGC signals that occurred within an eight BCID (200 ns) window were read out. The timing between the scintillator coincidences and the readout window was calibrated so hits on the chamber from a triggering muon would be centred in the readout window.

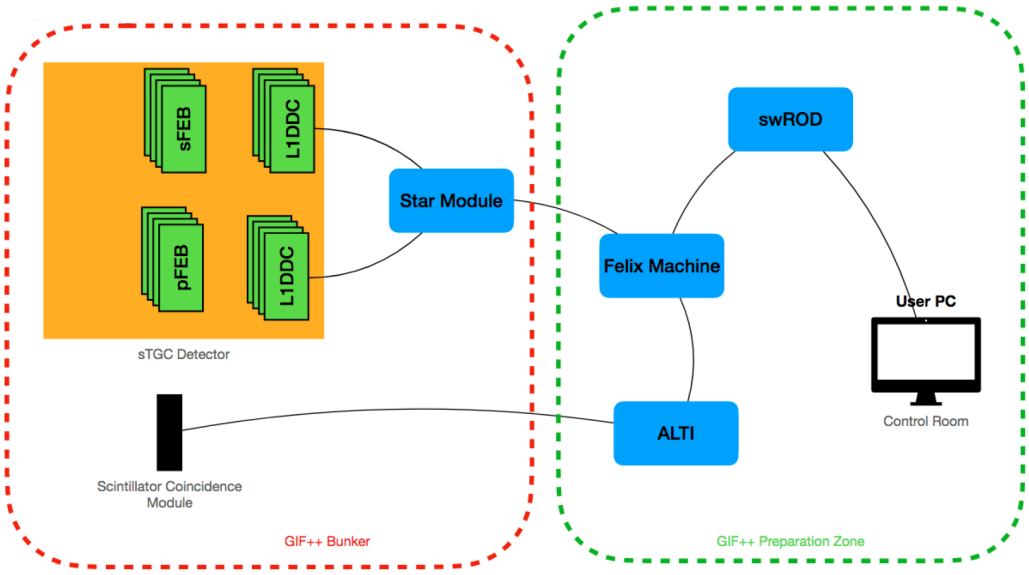

Figure 5.3: Simplified trigger and readout chain used for the sTGC 2021 test beam. Figure courtesy of Gerado Vasquez.

5.3 sTGC test beam goals

The motivation for conducting the test beam for the sTGC community was to study the effects of different readout parameters, detector functionality, and efficiency with varying levels of background. The nature of the GIF++ facility offered various testing

conditions during the data collection period, with a range of known background rates and a muon beam.

The sTGC has two primary functions: triggering and precision track reconstruction. The pads need to be able to measure charge deposition with a high enough threshold to cut low energy background particles while allowing the chambers to be sensitive to charged particles traversing the sTGC, with those tracks producing hits in multiple layers of pads. The test beam data was used to study the signal strength (Section 5.6) and efficiency of the pads as a function of background and high voltage setting.

The test beam also allowed for the charge clustering and track reconstruction capability of the strips to be studied. The strips must be able to measure charge depositions that are spread across multiple strips and reconstruct charged tracks. The position of a hit on a single strip must be assigned to centre of the readout strip. The difference between the true and measured position of the hit follows a Gaussian distribution. The uncertainty in position is given by:

$$\sigma^2 = \int_{-p/2}^{p/2} \frac{x^2}{p} dx = \frac{p^2}{12} \tag{5.1}$$

The position resolution of a single strip with a pitch p is thus $p/\sqrt{12}$ [27]. As the strip pitch is 3.2 mm, this resolution would be quite poor. For this reason, the neighbors feature of the strips (see Section 3.5.1) was designed to ensure that muon hits nearly always result in a charge cluster spread across at least three strips. The centre of the charge distribution is calculated via a centroid method, which results in a resolution of about 100 μm.

5.4 Data Collection

Various operational and readout parameters were tested during the data collection. Data was collected with the muon beam and with the gamma source using attenuation factors of 1, 1.5, 2.2, 3.3, 4.6, 6.9, 10, 15, 22, 46, and 100. This ensured that data was collected over a range of background rates, from 0 to 13 kHz/cm^2, allowing for observation of the sTGC performance as a function of background rate. Two peaking times (described further in Section 3.5.1), 25 and 50 ns, were utilized in data collection to observe the impact a shorter integration period had on efficiency and charge cluster

reconstruction.

The nominal operating high voltage setting for the sTGCs in the NSW is 2800 V. During the test beam, the chamber was operated at high voltages ranging from 2750 V to 2950 V, in increments of 25 V, to test the efficiency as a function of voltage. These high voltage scans were conducted for both peaking time settings over a range of backgrounds.

As discussed in Section 5.3, the neighbors feature of the strips increases the resolution by digitizing charge from below-threshold signals for strips adjacent to strips with above-threshold signals, which increases the number of strips included in a charge cluster. In order to quantify the improved resolution, data was collected with the neighbors feature on and off.

A majority of the data was collected using the GIF scintillators for triggering, with detector read out following a coincidence from the two scintillators. Data were also collected using combined triggers from the smaller sTGC scintillators and the GIF scintillators. The pad efficiency was studied using the data collected from the four-scintillator coincidence runs, as the majority of muon hits on the sTGC should have been focused within a single logical tower. For the studies in Section 5.6, data collected with the 25 and 50 ns peaking time and a range of HV settings over various background rates were utilized, with coincidences from the GIF scintillators as triggers. Track reconstruction was also tested by tilting the quad, with data collected at 0, 10, and 20 degrees and a range of background rates.

An event is the set of data read out following a single trigger from the scintillators. The number of events recorded in a given run depended on the particular data collection goal for the day, the schedule for attenuation filters, the stability of the data acquisition system, as well as the beam intensity and stability.

5.5 PDO and Charge Calibration

Energy deposition in the sTGC is measured by the digitized value of the integrated charge, the Peak Detector Output (PDO), where PDO is the height of a signal over the threshold for a channel. As discussed in Section 3.5.1, the VMM has a 10-bit ADC converter which has 1024 (2^{10}) unique digital values for PDO, which is measured in ADC counts. Any extremely large signals that exceed the maximum digitized value are recorded as 1024 PDO. For this reason, there are artificial peaks at the last PDO value that needed to be excluded from this analysis.

The thresholds for the sTGC channels (every strip, pad, and wire group) during the test beam were set as an offset from the baseline, where the baselines were measured during a period with no beam and the source off. The pad thresholds (set in DAC units above baseline, which can be converted to mV above baseline) were user-modified from the nominal offset from baseline (approximately 45 mV above baseline) in order to calculate the conversion between charge and PDO. Data was collected at 7 different pad threshold values from approximately 45 to 70 mV at an attenuation setting of 1.5. A 2D histogram of PDO vs the threshold offset (in mV) can be seen in Figure 5.4 for one of the pads in the centre of the beam. As can be seen in the plot, the lower bound of the measured PDO steadily rises as the threshold is increased, as expected.

The source-on data (which gave the widest energy range of charge deposition) with the varied threshold values were used to find the threshold PDO value for each pad in the beam area. The PDO threshold that was selected was the lowest PDO value (x) where it and the next PDO value (x+1) had at least 5 hits. This method is to avoid selecting values as the threshold that resulted from a charge integration error, where analog-to-digital conversion process is terminated early, and were artificially lower than the true value, such as the single low PDO values seen at 56 and 60 mV in Figure 5.4.

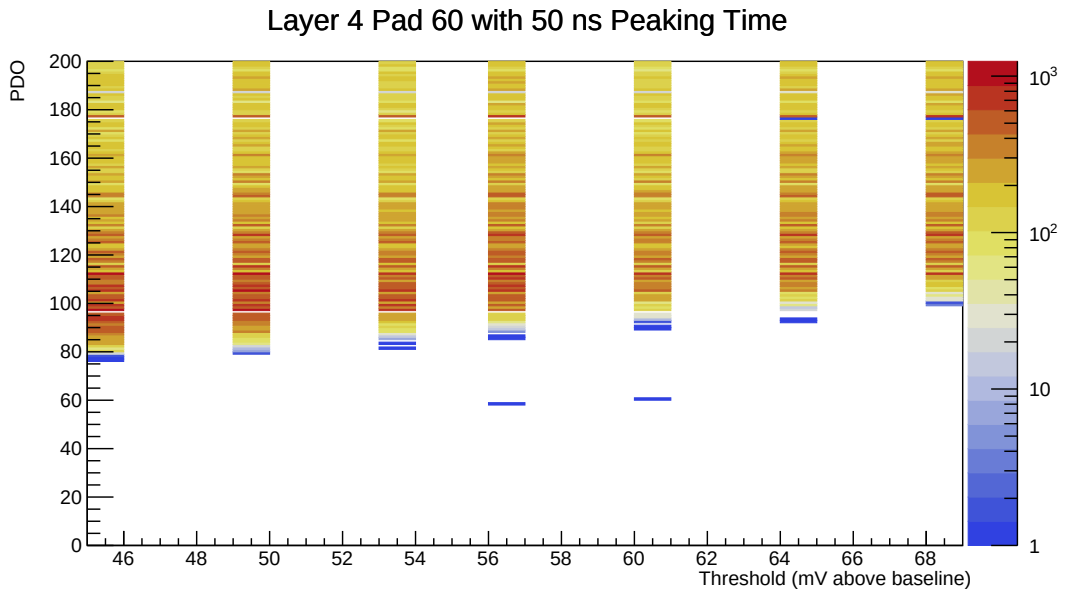

Figure 5.4: The PDO vs threshold distribution for a pad in the centre of the beam, on the first pad layer.

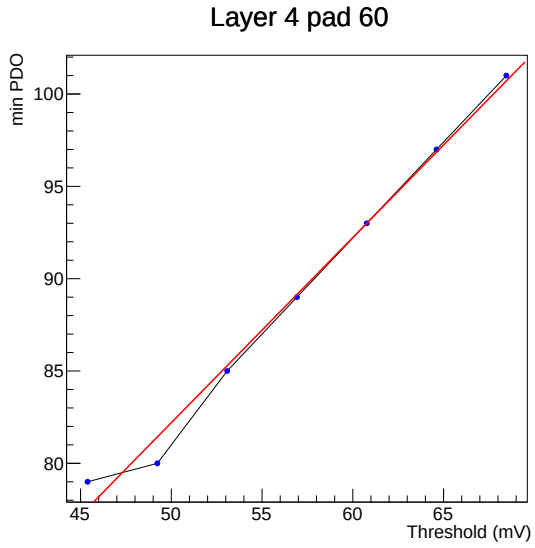

Figure 5.5: The calibration of PDO to mV by fitting the minimum PDO vs threshold for a pad in the centre of the beam, on the first pad layer. The minimum values are given by the blue markers and the fit by the red line. The y-value of the fit at the nominal threshold (45 mV) was utilized as the threshold in PDO for these studies.

Once the minimum was found for every threshold value, a plot (for each pad within the beam) of minimum PDO vs threshold was produced and these minimum values were fit to a line. An example of the minimum PDO plotted as a function the threshold for a single pad is shown in Figure 5.5. The fits on average had a slope of 1.04 ± 0.09, with the y-intercept, which should be approximately equal to the baseline, varying per pad. The calibration from PDO to mV is (PDO-intercept)/slope and uncertainties on PDO are converted to mV by dividing by the slope. This calibration method is similar to the calibration used for charge distributions on the strips.

5.6 Landau Peak Studies

Massive, charged, fast particles traversing a thin layer of material deposit energy via ionization in a random process [28]. Most particles only lose a small fraction of particle energy to ionization, so the energy distribution is skewed by rare hard interactions (e.g. bremsstrahlung). The energy deposited by these minimum ionizing particles (MIP) passing through thin detectors is described by a Landau function, an asymmetric distribution with a sharp peak and a long tail.

The Landau distribution is very asymmetric, with an undefined mean [28]. Exam-

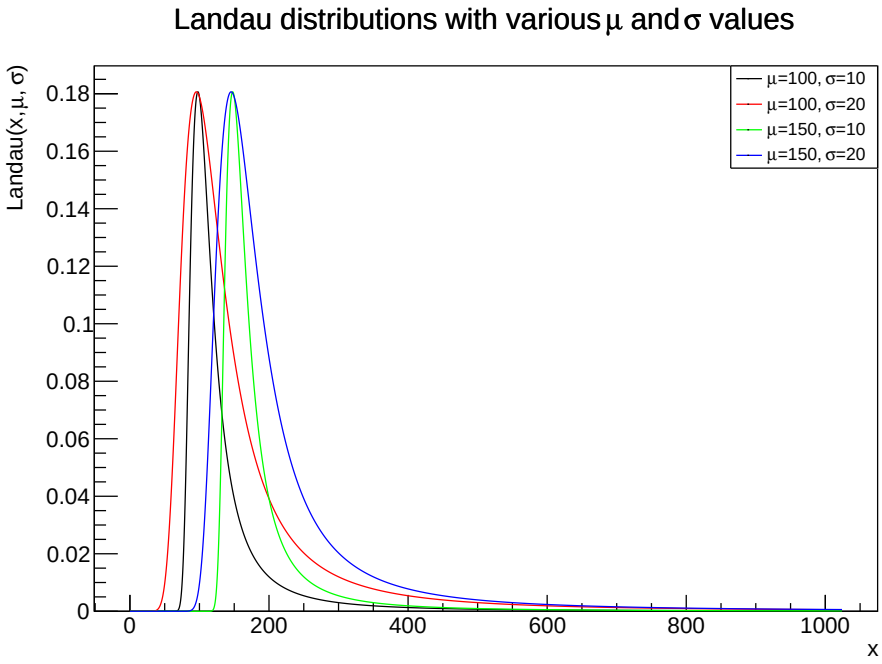

Figure 5.6: Examples of Landau distributions with two location parameters and two width values. As the black and red (blue and green) curves have the same location parameter $\mu = 100$ ($\mu = 150$), the two curves peak at the same x-value. The width parameter σ determines the shape of the rising and falling edges of the distributions.

ples of Landau distributions are shown in Figure 5.6 to illustrate the effect of the two parameters. As a result, the practical descriptors of a Landau distribution are the width parameter σ and the location of the peak, the Most Probable Value (MPV).

The aim of this analysis was to characterize the sTGC pad response to a minimum ionizing muon, which was accomplished by fitting the PDO distribution from each pad in the muon beam (those with the borders in Figure 5.7) to a Landau function and obtaining MPVs from these fits. Using the MPVs from data collected at various background rates, high voltage settings, and integration times, we can observe how these parameters affect the signal strength and pad response. The results from this test beam analysis provide estimates on the functionality of the sTGCs within ATLAS that will inform decisions on the ideal operating settings during Run 3 and the HL-LHC. It has been suggested that increasing the high voltage might compensate for the signal degradation due to increasing backgrounds. This study in particular is focused on data-noise separation; measuring clear muon signals that are distinguished from background.

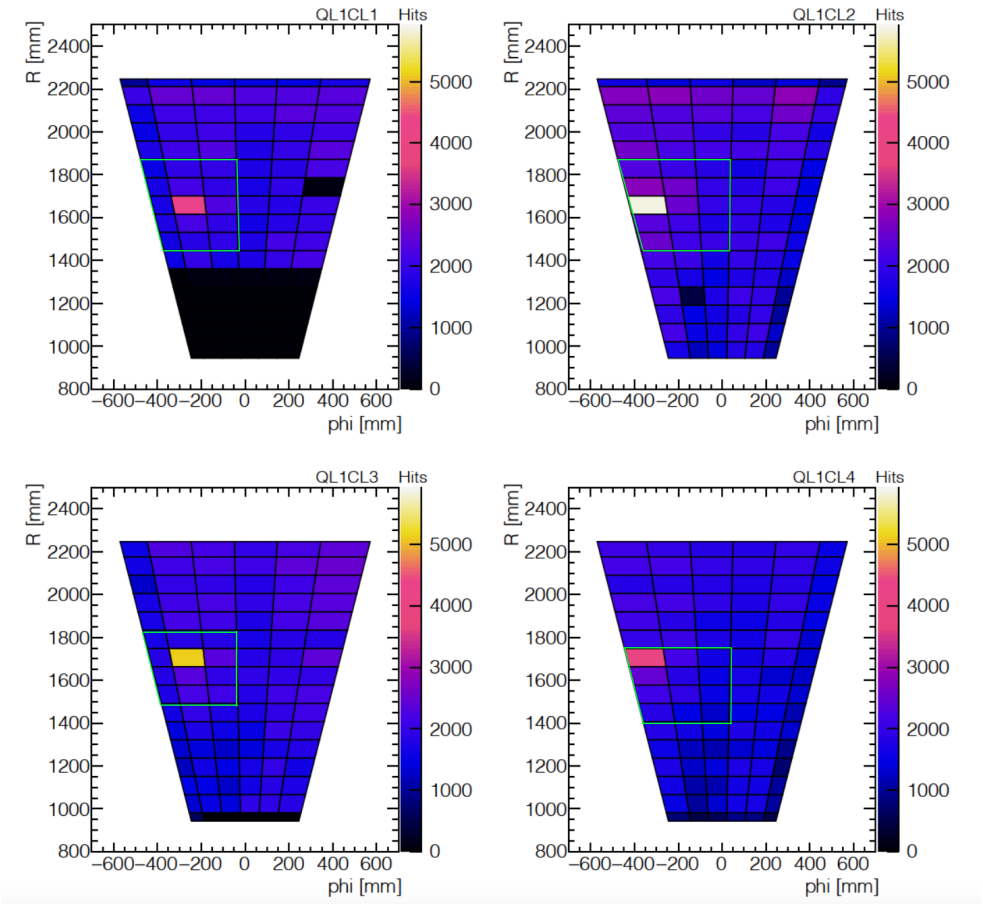

Figure 5.7: Distribution of pad hits from one attenuation 1 run. The pads selected for analysis are within the green boxes, around the muon beam position.

5.6.1 Coincidence Requirements

The raw PDO distributions from runs with high background rates did result in good Landau fit results. The gamma source produced a near uniform background distribution of pad hits on the tested module. In order to reject a majority of these background hits and consider only charge from muons, pad hits (and corresponding PDOs) were selected that could be matched to a three or four-layer coincidence, using the pattern matching methods described in Chapter 4 as well as the timing requirements described in Section 4.3. The aim was that the pad pulse height (PDO) distributions with the source on were originating from the muon beam and that background from the gamma source could be cut from the muon signal.

With this coincidence requirement implemented, the Landau fits for the runs with high background improved. The distribution of pad hits with the muon beam

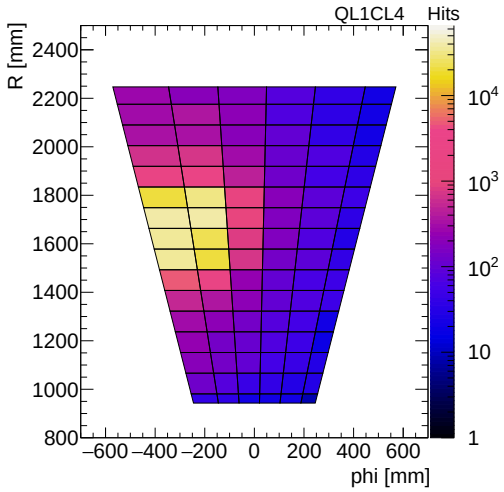

Figure 5.8: Heat maps of hits on the test module with high voltage setting of 2800 V and no source. Most muon hits are clustered on a few pads. The rate of muon hits on pads drops exponentially for pads away from the centre of the beam. As the data was collected following coincidences from the large GIF scintillator modules, there was a large spread of muon tracks that could produce triggers and pads away from the beam centre recorded muon hits.

alone (Figure 5.8) resemble the distribution of hits after applying coincidence cuts on Attenuation 100 data (Figure 5.9). The implication of these two distributions is that, at low background rates (.13 kHz/cm^2), there were almost no individual γ-ray interactions within the sTGC that produced track-like hits in multiple layers. At high photon rates, track-like events may result from multiple photons traversing the same logical tower and interacting with different layers, producing what appear to be hits in coincidence (Figure 5.10).

5.6.2 Landau Fits

For these studies, the data from all available runs (taken with the GIF scintillator coincidence) with identical conditions (high voltage setting, background rate) were merged after the event-specific cuts were applied. For each event, only pad hits that form logical towers containing 3 or 4 layers of pads were considered for the Landau analysis. Pad hits were required to be within the centre of the readout window in order to ensure that the hits were most likely due to a beam muon. The PDO values from these accepted pad hits, for the pads that were within the beam were binned into histograms, with separate histograms for each pad and run condition (peaking

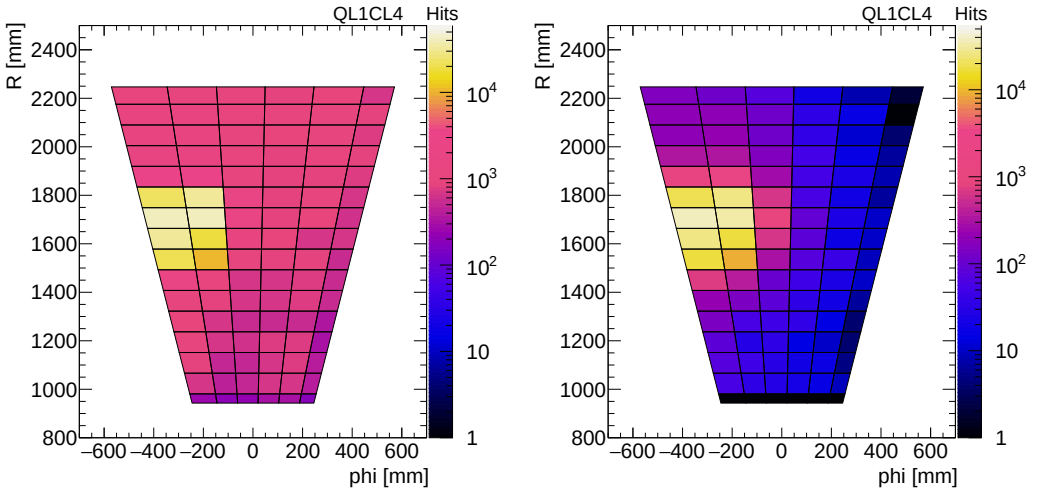

Figure 5.9: Distribution of pad hits before (left) and after coincidence cuts (right) are applied for test beam runs with a 50 ns peaking time, attenuation 100.0 and 2800 V high voltage setting. After the coincidence cut is applied, the region of pads within the beam is clearly distinguishable.

time, high voltage, and attenuation). The fraction of pad hits rejected by each cut is shown in Table 5.1.

Type of cut	Min. % of hits cut	Max. % of hits cut
No 3/4 or 4/4 coincidence	11%	97 %
Not within the beam	4%	56%
relBCID <2 or > 5	0.05%	19%

Table 5.1: Maximum and minimum percent of hits rejected by various cuts; showing the percentage of hits rejected at each stage of cut. Hits were rejected for not being in coincidence, from pads outside of the beam region, and for being out of the centre of the readout window.

The PDO histograms (Figure 5.11) had a bin-width of 16 PDO counts in order to mitigate the effect of spikes in channels caused by known digitization errors with the 10-bit ADC (where the conversion stopped with the component of 6-bit ADC, missing the last $2^4 = 16$ granularity). The lower edge of the first bin of a histogram was the estimated threshold in PDO for the corresponding pad. This ensured that the first measured bin of the rising edge of the Landau distribution was not truncated artificially by including empty bins below the threshold, which can strongly deform the Landau fits. The motivation for this binning procedure is further explained in Appendix A.2.

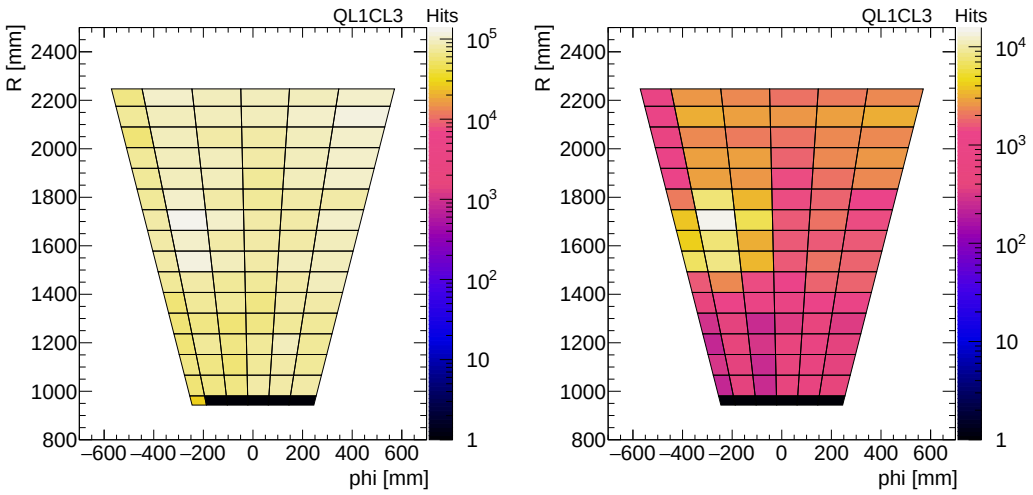

Figure 5.10: Distribution of pad hits before (left) and after coincidence cuts (right) are applied for test beam runs with a 50 ns peaking time, attenuation 1.0 and 2800 V high voltage setting.

In order to avoid fitting histograms with low statistics, only histograms that exceeded a minimum threshold for number of entries were fit to a Landau distribution [29]. The threshold for a given run type was set at 10% of the number of entries in the histogram with the greatest number of entries for that run type. Examples of PDO distributions with Landau fits are shown for an individual pad in Figure 5.11. From the fit, the Most Probable Value is obtained. Fits that failed to converge or had non-physical MPVs (fit failed to find the peak of the distribution) were rejected. For fits that met the above conditions, the MPV and associated error on the MPV from the fit were calibrated using the methods described in Section 5.5.

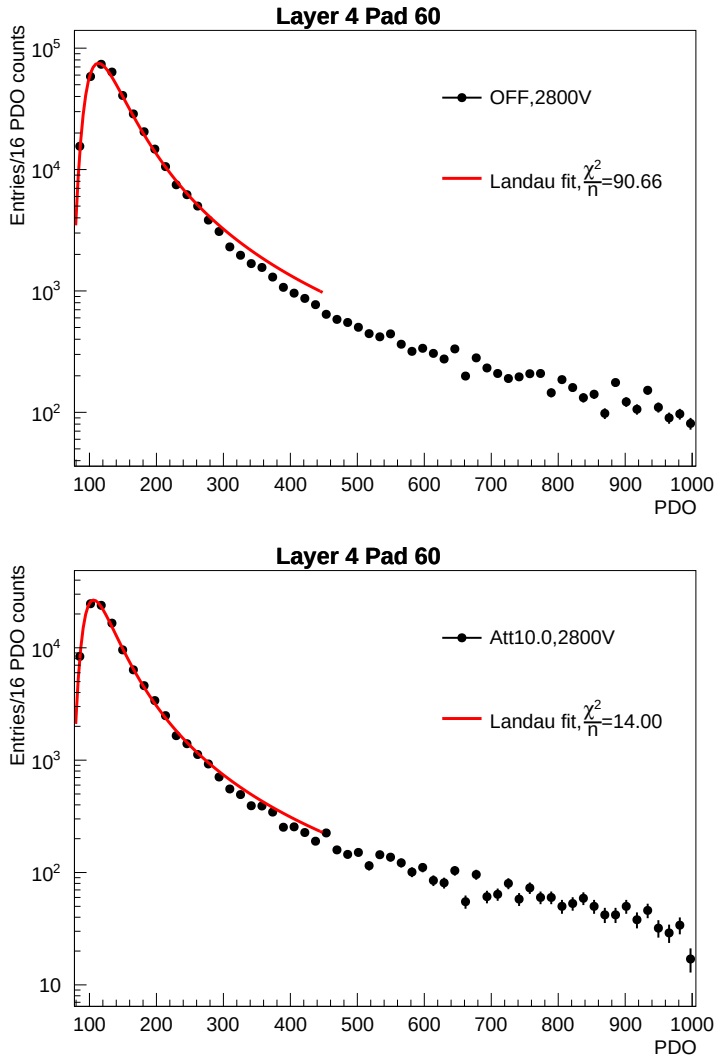

Figure 5.11: PDO distributions with 50 ns peaking time for the pad in the centre of the beam on the layer closest to the gamma source of the sTGC with a high voltage setting of 2800 V. The distribution with no source (top) peaks at higher PDO values than the source-on distribution (bottom). This is expected because the background hits generate a current that lowers the local high voltage as described in Section 5.8

5.7 MPV Comparisons and Trends

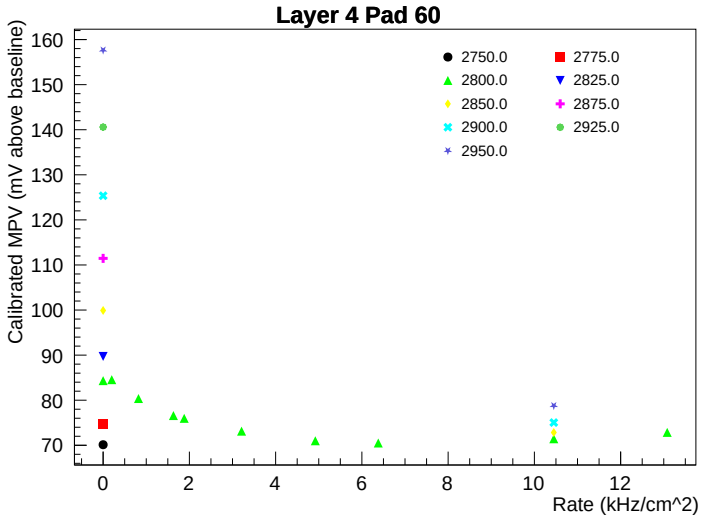

Figure 5.12: Calibrated MPV values with 50 ns peaking time for the pad in the centre of the beam at various high voltage settings and background rates. The error bars corresponding to the fit uncertainty on the MPVs are smaller than the markers.

The accepted (MPVs that met the requirements described in Section 5.6.2) and calibrated MPVs for each pad in the beam region (as given in Figure 5.7) were plotted against rate (Figure 5.12) and high voltage (Figure 5.13). On an individual pad basis, the effect of raising the high voltage can be seen in an increase in MPV, while the higher background rate results in lower MPV. In Figure 5.13, the gain in signal strength due to increasing the high voltage is much lower at the high background (attenuation 1.5) than when the source is off.

For a given pad, let n_i be the number of hits on the pad that were matched to a coincidence, with i ranging over the number of pads with corresponding Landau fits that passed the selection criteria. Then let N_{tot} be the sum of n_i over the range of i. The weight factor w_i for the fitted MPV of a given pad is

$$w_i = n_i / N_{\text{tot}} \tag{5.2}$$

The weight factor defined above was used to fill weighted MPV histograms where each bin is the mV equivalent of 5 PDO counts. An example is given in Figure 5.14. The weighted histograms were fit to Gaussian distributions and the means from the fits that converged with a peak with a location greater than zero were plotted against

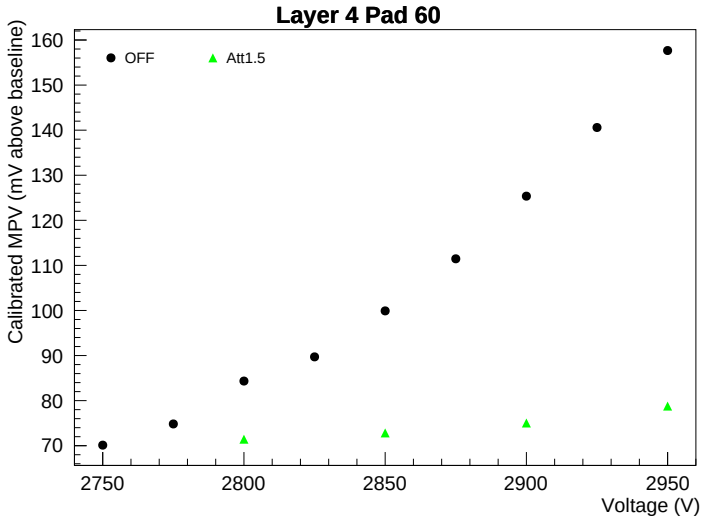

Figure 5.13: Calibrated MPV values with 50 ns peaking time for the pad in the centre of the beam on the first layer with the sTGC at various high voltage settings taken with the source off and with the source on (attenuation 1.5).

high voltage or background rate, which is shown for 50 ns peaking time data in Figure 5.15. The uncertainties on the Gaussian means are the errors from the fit parameter.

Another comparison plot is shown in Figure 5.16, where the statistical average values of the MPVs (that met the requirements described in Section 5.6.2) from the pads in the beam area are plotted against voltage for the various background attenuation factors, with a 50 ns peaking time. The uncertainty on the average values is the standard deviation.

The final comparison plot, given in Figure 5.17, plots the weighted mean values of MPVs against the HV setting. The uncertainty on the MPV M_i, σ_i, is the error on the MPV in the Landau fit. For MPVs M_i with corresponding weights w_i (as defined in Equation 5.2), the weighted mean is

$$\overline{M} = \frac{\sum_i w_i M_i}{\sum_i w_i} = \sum_i w_i M_i, \tag{5.3}$$

as

$$\sum_i w_i = \sum_i \frac{n_i}{N_{\text{tot}}} = \frac{\sum_i n_i}{\sum_j n_j} = 1. \tag{5.4}$$

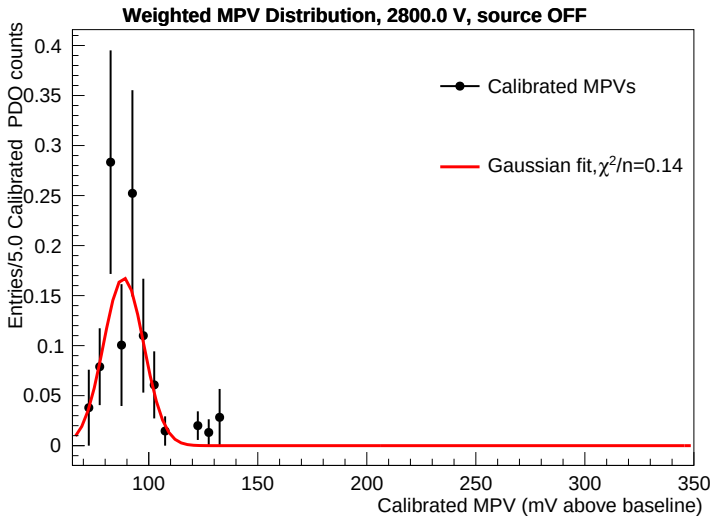

Figure 5.14: Histogram filled with MPV values, weighted by the fraction of hits in three out of four or four out of four coincidence for 50 ns peaking time data, source off, and 2800 V high voltage setting. The histogram was fitted with a Gaussian distribution.

The uncertainty on $\overline{M}$ is

$$\overline{\sigma} = \frac{\sqrt{\sum_i w_i^2 \sigma_i^2}}{(\sum_i w_i)^2} = \sqrt{\sum_i w_i^2 \sigma_i^2}. \tag{5.5}$$

The weighted mean MPVs are plotted for the 50 ns peaking time in Figure 5.17. The MPV trends as a function of background rate are shown in Figure 5.18. While the 2800 V data shows that MPV drops with increasing background rate, the drop stabilizes at high rates. Unfortunately the gain in MPV from increasing high voltage diminishes at high background rates.

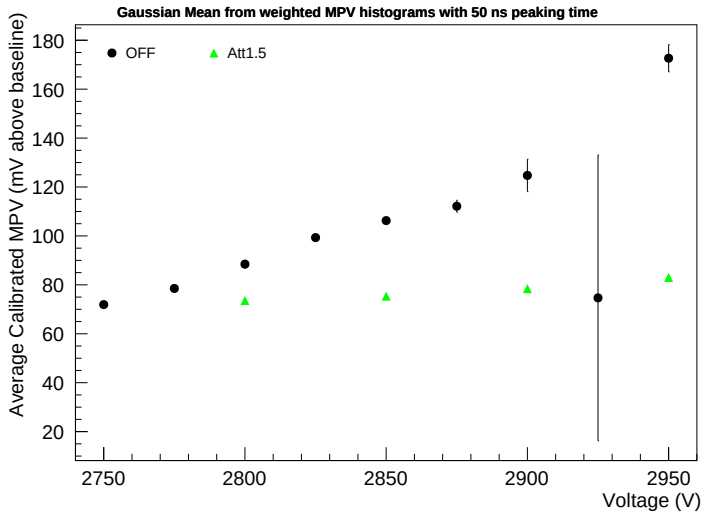

Figure 5.15: Gaussian means from weighted MPV histograms for 50 ns peaking time. The fit for the source off, 2950 V weighted MPV distribution returned a Gaussian mean that was far lower than the average MPV.

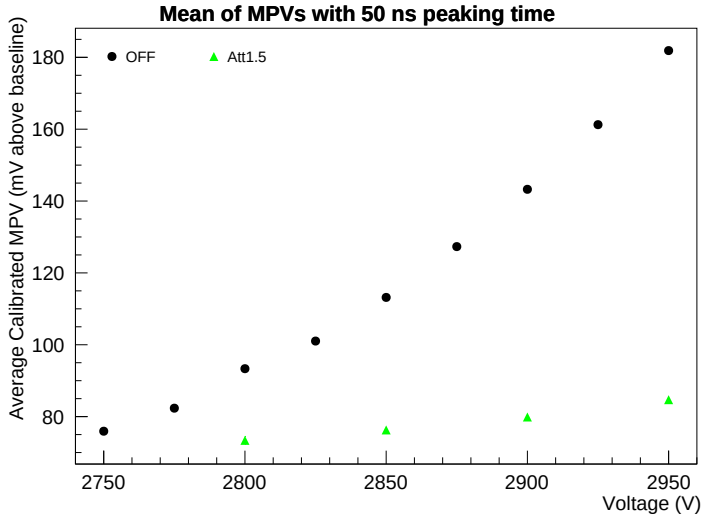

Figure 5.16: Distribution of mean MPVs against high voltage setting for 50 ns peaking time. The uncertainties of the mean MPVs with source off are smaller than the markers.

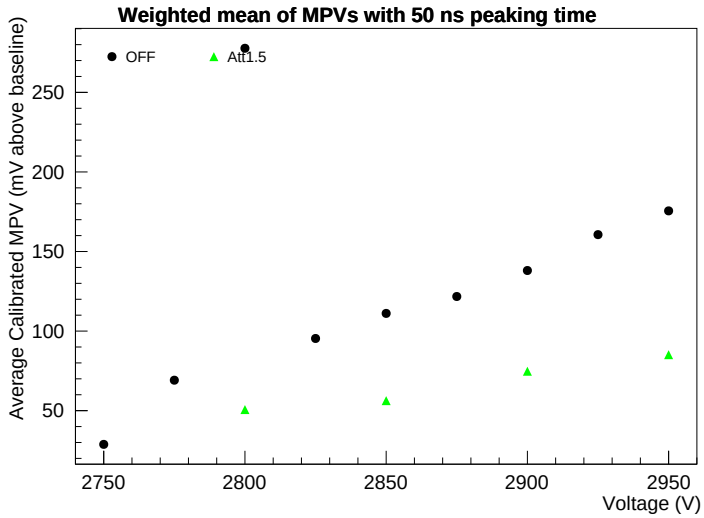

Figure 5.17: Distribution of weighted mean MPVs against high voltage setting for 50 ns peaking time. Increasing the applied high voltage always results in an increased signal response, but the increase diminishes in the presence of background.

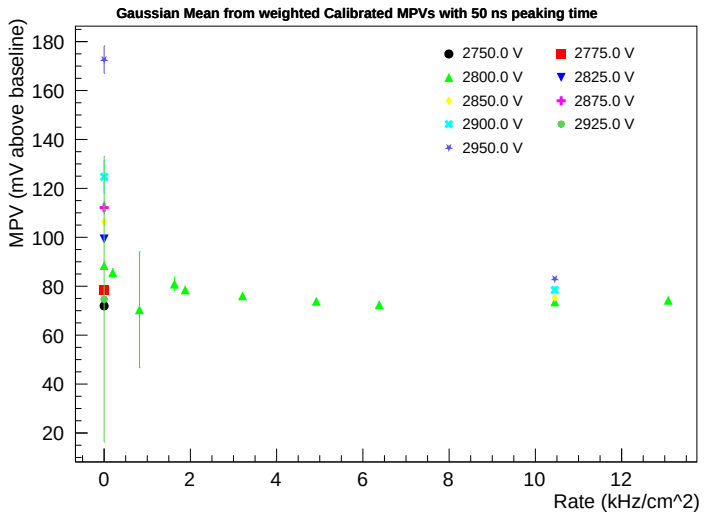

Figure 5.18: Gaussian means from weighted MPV histograms for 50 ns peaking time, plotted against background rate.

5.8 Effects of Gamma Background

The gamma background in the test beam originates from the ^{137}Cs source which emits photons with energies of 662 keV and 32 keV [26]. The higher energy gamma rays primarily deposit energy via photoelectric absorption. Any photons that interact with the sTGC are either completely absorbed, scatter inelastically (Compton scattering), or scatter elastically at extreme angles (Rayleigh scattering), as the emitted gamma rays are not energetic enough to pair-produce. Photon interactions via the photoelectric effect or Compton scattering result in detectable scattered electrons: if the energy is sufficient to reach the gas volume, these can be detected with nearly 100% efficiency. The sensitivity of a single TGC layer to the 662 keV gamma rays emitted by ^{137}Cs was found to be less than 1% [30].

Studies that simulated X-ray interactions with the sTGC found that photoelectrons (the electrons emitted from photo-absorption) are typically created in the anode wires, graphite layer and gas mixture, with most Compton electrons produced in the gas mixture and copper ground layers and strips [31]. The Compton electrons produced by X-rays in the sTGC were found to have very low kinetic energies and were only able to travel very short distances. As the X-rays modelled in that study had much lower energies (maximum 50 keV) than the gamma rays, the results are not completely applicable to the test beam.

The 662 keV gamma rays might be able to produce secondary electrons with sufficient energy to traverse and be detected in multiple layers of the sTGC. With the low (1%) sensitivity to gamma detection, it is unlikely for a single gamma ray to produce secondary electrons in multiple layers of the sTGC. However, a sufficiently energetic secondary electron might be able to traverse multiple gas volumes and produce signals in coincidence.

As a means of visualizing the potential for a photon to produce track-like signals in the sTGC, two pad hit heat maps with a low background rate (0.13 kHz/cm^2) were produced. The heat map on the left in Figure 5.9 is from all pad hits on Layer 7 (QL1CL4), while the map on the right is for only the pad hits on the same layer that were found to be part of a three out of four or four out of four coincidence. It is notable that the post-cut heat map looks nearly indistinguishable from the heat map in Figure 5.8 which was created from pad hits with no gamma background and no cuts applied. The implication of these two heat maps is that an individual photon is unlikely to create hits in coincidence. Then, considering the heat maps produced

without and with coincidence cuts from pad hits in a high background environment (13 kHz/cm^2), the high number of pad hits in the area outside of the muon beam after the coincidence cut was applied suggests that multiple photons are traversing the same logical towers simultaneously, producing the appearance of a coincidence from a charged track.

From the average MPV vs background rate plot (Figure 5.18), it is clear that the signal strength is inversely related to the background rate. The higher rate of gammas interacting with the sTGC results in a higher rate of secondary electrons and ionization charge. The high rate of ionization causes a charge buildup on the cathodes and an effective voltage drop.

In addition to the charge deposition effects, the dead time implemented in the sTGC setup meant that many pads that should have been able to detect a beam muon had been recently fired by a gamma and were thus unavailable. With fewer channels capable of registering hits, the rate of hits with a logical tower decreases with increasing background, as is shown in Figure 5.19. At high rates, not only are pads recording less hits in coincidence from true muons, they could potentially trigger on coincidences caused by background. The three-out-of-four and three-out-of-four requirement used by the Pad Trigger should eliminate the majority of these false triggers occurring in the NSW.

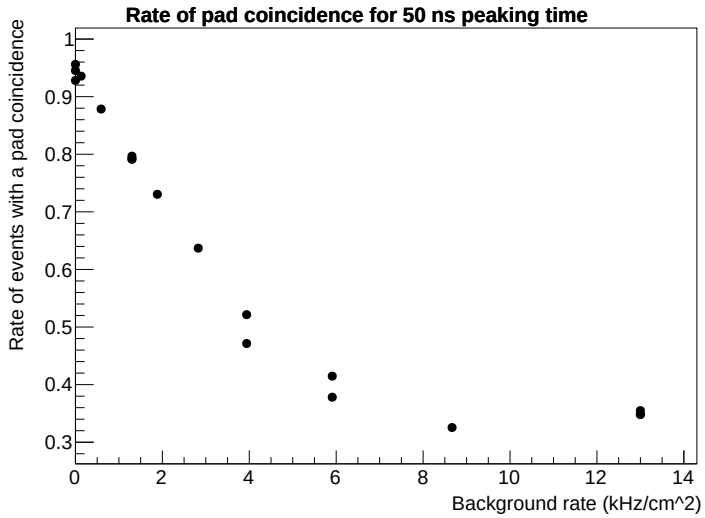

Figure 5.19: Fraction of three out of four and four out of four coincidences for 50 ns peaking time, 2800 V high voltage setting. The fraction of events with a coincidence drops with increased background rate. Runs with identical background rates are presented here as separate data points.

5.9 Results

Considering both the trends for individual pads and averaging over accepted MPVs for pads in the beam region, we can see that as the sTGC is operated with increasingly higher voltages, we observe a rise in MPV. This is expected as a higher HV setting will result in a higher gain and thus a larger signal. Conversely, when the high voltage setting is fixed, we observe the MPV falling as the background rate increases. While operating the chamber at a higher voltage helps to recover some of the signal strength that is lost at a high background, the loss of strength at the high background rates is greater than the recovery effect.

Preliminary measurements suggest that the highest background rate available at GIF++ may be greater than the highest background rate that any part of the NSW will experience during the HL-LHC. The sTGC may be able to recover some efficiency loss from the background by operating the chambers at a greater high voltage setting, however the degradation of the signal due to background cannot be completely compensated for by simply increasing the high voltage.

Chapter 6

Conclusions

The pads of the sTGCs provide efficient initial triggers for the NSW. The logical tower design allows for a relatively large pad to have four separate triggering regions, when pad hits on multiple layers are considered in coincidence. This reduces the number of readout channels needed for the pad plane while still providing fast triggers and input to precision track reconstruction. The two wedges with four gas volumes allow for potential trigger candidates to have two out of eight missing layers while still providing fast and precise track information. This allows for the NSW to trigger on muons originating from the IP and provide confirmation of tracks triggered in the Big Wheels.

The strength of the pad signals is strongly dependent on high voltage and background rate. While the strongest signals produced in the pads occur when there is no background, the pads are still able to reconstruct muons signals at high background rates. In a low background environment the sTGC pads are extremely responsive to increases in high voltage, with great gains in signal strength. The signal strength falls as the background rate increases, but increasing high voltage may help to partially recover lost signal strength.

By providing triggers in the inner end-cap region, the NSW will eliminate the majority of fake muon triggers in the end-cap, allowing the L1 muon trigger threshold to remain at a relatively low-p_T. While Run 3 has just begun, the NSW is an exciting addition to ATLAS that will allow the detector to continue to trigger on the muons from the production of Higgs or gauge bosons and other physics events of interest.

Bibliography

[1] The CMS Collaboration. Observation of a new boson at a mass of 125 GeV with the CMS experiment at the LHC. Physics Letters B, 716(1), September 2012.

[2] The ATLAS Collaboration. Observation of a new particle in the search for the Standard Model Higgs boson with the ATLAS detector at the LHC. Physics Letters B, 716(1), September 2012.

[3] The ATLAS Collaboration. The ATLAS experiment at the CERN Large Hadron Collider. Journal of Instrumentation, 3(08):S08003, Aug 2008.

[4] CERN: Our History. https://home.cern/about/who-we-are/our-history. Accessed: 2022-8-08.

[5] CERN:Our Member States. https://home.cern/about/who-we-are/our-governance/member-states. Accessed: 2022-8-03.

[6] CERN's accelerator complex. https://home.cern/science/accelerators/accelerator-complex. Accessed: 2022-8-03.

[7] The Large Hadron Collider. https://home.cern/science/accelerators/large-hadron-collider. Accessed: 2022-8-09.

[8] Longer term LHC schedule. https://lhc-commissioning.web.cern.ch/schedule/LHC-long-term.htm. Accessed: 2022-11-08.

[9] The ATLAS Collaboration. The ATLAS experiment at the CERN Large Hadron Collider: A description of the detector configuration for Run 3. to be submitted to JINST, 2022.

[10] High-Luminosity LHC. https://home.cern/science/accelerators/high-luminosity-lhc. Accessed: 2022-8-22.

[11] Accelerating: Radiofrequency cavities. https://home.cern/science/engineering/accelerating-radiofrequency-cavities. Accessed: 2022-8-22.

[12] LHC Facts and Figures. https://home.cern/resources/brochure/knowledge-sharing/lhc-facts-and-figures. Accessed: 2022-8-09.

[13] T. Kawamoto, S. Vlachos, L. Pontecorvo, J. Dubbert, G. Mikenberg, P. Iengo, C. Dallapiccola, C. Amelung, L. Levinson, R. Richter, and D. Lellouch. New Small Wheel Technical Design Report. Technical Report CERN-LHCC-2013-006. ATLAS-TDR-020, CERN, Jun 2013. ATLAS New Small Wheel Technical Design Report.

[14] M. Tanabashi et al. Review of particle physics. Phys. Rev. D, 98:030001, Aug 2018.

[15] The ATLAS Collaboration. ATLAS Muon Spectrometer: Technical Design Report. Technical report, CERN, Geneva, 1997.

[16] The ATLAS Collaboration. Technical design report for the ATLAS Muon Spectrometer Phase-II upgrade. Technical Report CERN-LHCC-2017-017, CERN, December 2017.

[17] Juan Cristóbal Rivera Vergara. Cosmic ray tests for the QS1 module of the New Small Wheel in the ATLAS experiment and prospects on the search for heavy vector triplet bosons in the leptonic decay channels with the ATLAS experiment at the HL-LHC, 2018. Thesis, Pontificia Universidad Católica de Chile.

[18] George Iakovidis. VMM - an ASIC for Micropattern detectors. EPJ Web Conf., 174:07001, 2018.

[19] The ATLAS Collaboration. The VMM3a user's guide. Technical Report ATL-MUON-PUB-2022-002, CERN, April 2022.

[20] P. Moreira, A. Marchioro, and Kloukinas. The GBT: A proposed architecure for multi-Gb/s data transmission in high energy physics. http://cds.cern.ch/record/1091474, 2007.

[21] Peter K.F. Grieder. Cosmic Rays at Earth. Elsevier, Amsterdam, 2001.

[22] High energy cosmic rays striking atoms at the top of the atmosphere give the rise to showers of particles striking the Earth's surface. http://cds.cern.ch/record/40407, May 1999.

[23] Evan Michael Carlson. Results of the 2018 ATLAS sTGC test beam and internal strip alignment of sTGC detectors. https://cds.cern.ch/record/2688394, 2018. Thesis, University of Victoria.

[24] M.R. Jaekel, M. Capeans, I. Efthymiopoulos, A. Fabich, R. Guida, G. Maire, M. Moll, D. Pfeiffer, F. Ravotti, and H. Reithler. CERN GIF++: A new irradiation facility to test large-area particle detectors for the high-luminosity LHC program. Proceedings of Science (TIPP2014), 102, 2014.

[25] GIF++. https://ep-dep-dt.web.cern.ch/irradiation-facilities/gif. Accessed: 2022-8-11.

[26] Dorothea Pfeiffer, Georgi Gorine, Hans Reithler, Bartolomej Biskup, Alasdair Day, Adrian Fabich, Joffrey Germa, Roberto Guida, Martin Jaekel, and Federico Ravotti. The radiation field in the Gamma Irradiation Facility GIF++ at CERN. Nuclear Instruments and Methods in Physics Research Section A: Accelerators, Spectrometers, Detectors and Associated Equipment, 866:91–103, 2017.

[27] Helmuth Spieler. Semiconductor Detector Systems. Oxford University Press, Aug 2005.

[28] L.D. Landau. On the energy loss of fast particles by ionisation. In D. Ter Haar, editor, Collected Papers of L.D. Landau, chapter 56, pages 417–424. Pergamon, 1965.

[29] ROOT::Minuit2::MnMigrad Class Reference. https://root.cern.ch/doc/master/classROOT_1_1Minuit2_1_1MnMigrad.html. Accessed: 2022-11-04.

[30] B. Ye S. Tsuno, T. Kobayashi. Gamma-ray sensitivity of a Thin Gap Chamber. Nuclear Instruments and Methods in Physics Research Section A: Accelerators, Spectrometers, Detectors and Associated Equipment, 482:667–673, 2003.

[31] Benoit Lefebvre. Characterization studies of small-strip Thin Gap Chambers for the ATLAS Upgrade. PhD thesis, McGill University, Aug 2018.

[32] K.S. Kölbig and B. Schorr. A program package for the Landau distribution. Computer Physics Communications, 31, 1984.

[33] ROOT::Math::VavilovFast Class Reference. https://root.cern.ch/doc/master/classROOT_1_1Math_1_1VavilovFast.html. Accessed: 2022-10-05.

[34] langaus.C File Reference. https://root.cern/doc/master/langaus_8C.html. Accessed: 2022-10-05.

Appendix A

Supplemental Information

A.1 Pad Tower Overlaps and Track Angles

In Figure A.1, a pad pattern corresponding to a logical tower is shown. The staggering of the pads can be seen clearly, with all four layers on the Confirm wedge offset so that their overlap is about one quarter of each pad. The overlap-finding script utilized pad corner data produced by the sTGC group at the University of Michigan. The script first considered two layers of pads and found the polygon that describes the overlap of the two pads. The overlap polygon was compared with each subsequent layer to find the area that lies within all four pads. Thus the area and coordinates of each four-layer logical tower were calculated.

The pad outlines, and the logical towers, are parallelograms with the upper and lower edges having fixed R-coordinates. The left and right edges are diagonal in the $R - \phi$ plane. When calculating the angular acceptance of a logical tower, the lower and upper edge (y_1 and y_2) and the distance (in z) between the first and fourth layer ($\Delta z = 33$ mm) are used to calculate the angle of a track that passes through the lower edge of the first layer and the upper edge of the logical tower:

$$\tan\theta = \frac{\Delta y}{\Delta z} \tag{A.1}$$

The angle θ is the maximum angle for tracks with coordinates increasing in R and Z (like IP-originating muons). For the Large sector logical towers, θ ranges from 39.6° to 63.3°, with an average angle of 50.9°± 5.8°. The average maximum track angle for the Small sector logical towers is 49.1°± 6.2°, with angles ranging from 36.9° to 61.3°. Cosmic rays do not have the same constraints on track coordinate

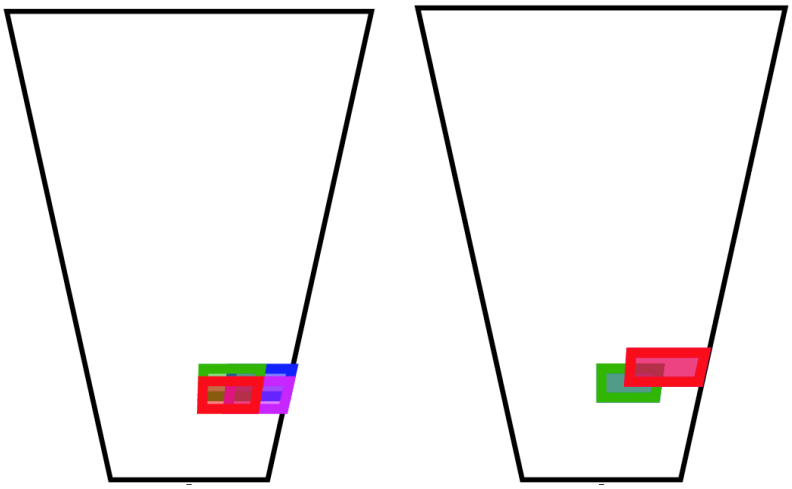

Figure A.1: An example of a logical tower on the inner small Confirm (left) and Pivot (right) wedges. The eight layer pattern is split over the two wedges and pad overlaps are calculated on a per-wedge basis. Each layer is coloured differently; layer 1 is blue, 2 is green, 3 is purple, and 4 is red. The pivot pad layers are symmetric, and therefore identical in layers 1 and 2 and layers 3 and 4.

behaviour as IP-originating muons. To account for tracks from cosmic rays, the angular acceptance θ must be multiplied by two, thus giving an average angular acceptance of approximately 100° for a four-layer pad pattern.

A.2 Landau Distributions Cut by Lower Bounds

Initially, the histograms utilized in the Landau studies were binned into bins of 16 PDO ADC channels from 0 to 1008. The final bin (PDO channels 1009 to 1024) included the ADC overflow bin 1024 and was excluded to avoid artificial peaks at the tail of the PDO distribution. In the course of the fixed high voltage Landau peak studies, we found that MPV tended to decrease as the background rate increased. However at background rates above 8 kHz/cm^2 (attenuations 1.5 and 1), the MPVs tended to increase, see Figure A.2. As the effective voltage drops with rate, MPV should not suddenly increase after falling consistently with the increased gamma rate. An explanation for this observation is that a combination of the effective voltage drop and lower energy depositions from gammas shifted the deposition distributions so that the peak of the distribution falls near or below the threshold, so that the peak and rising edge of the distribution were not digitized.

To model this effect, I used the Landau distribution from the ROOT TRandom3

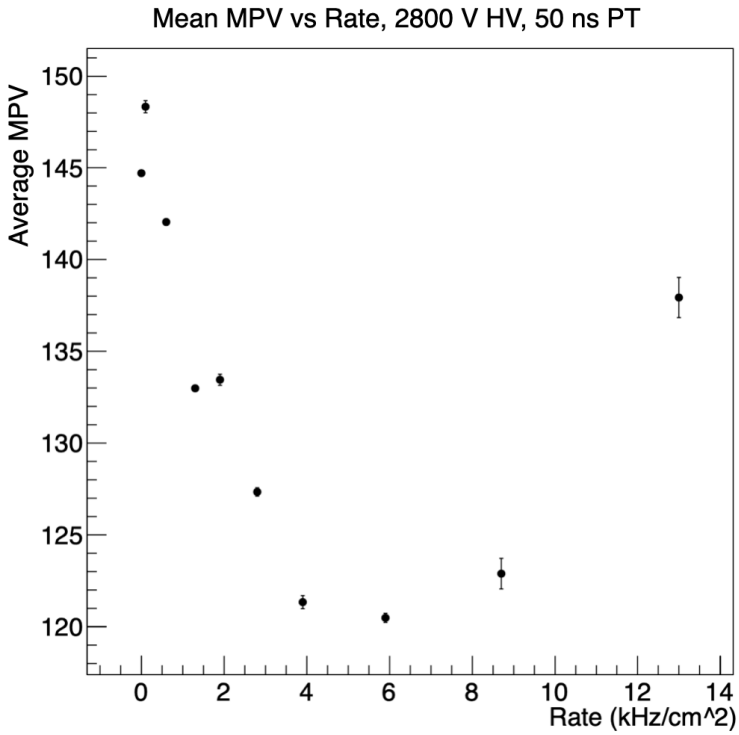

Figure A.2: Average MPV from initial binning method vs background rate for 2800 V high voltage setting and 50 ns peaking time (PT). The increase in average MPV at the highest background rates was highly suspect.

class, seeded by the Python pseudo-random number integer generator (randint from random) selected from 0 to 10,000. I then filled a histogram that was binned with the standard bin widths (16 count-wide, from 0 to 1008) with 10,000 pseudo-random values following a Landau distribution with similar μ[1] and σ as those found in hits of real data. In addition, using the same generated values, I filled two other histograms if the generated value was above a set threshold. One histogram had the standard binning starting from zero while the other had the lower edge of its first bin start at the threshold, and then proceed with 16 count-wide bins. All three histograms were then fitted to a Landau, using the same ROOT fitting methods as used in the other studies. Examples of the histograms are shown in Figure A.3 with a threshold of 60, μ of 50, and σ of 13.

In the modelled Landau distributions in Figure A.3, the histogram binned in the initial method with the threshold (red histogram) has the same bin boundaries as the

[1]The location parameter μ used to generate the Landau fits is related to, but not the same as the MPV. For an MPV of 0 and σ of 1, the corresponding μ is approximately -0.2.

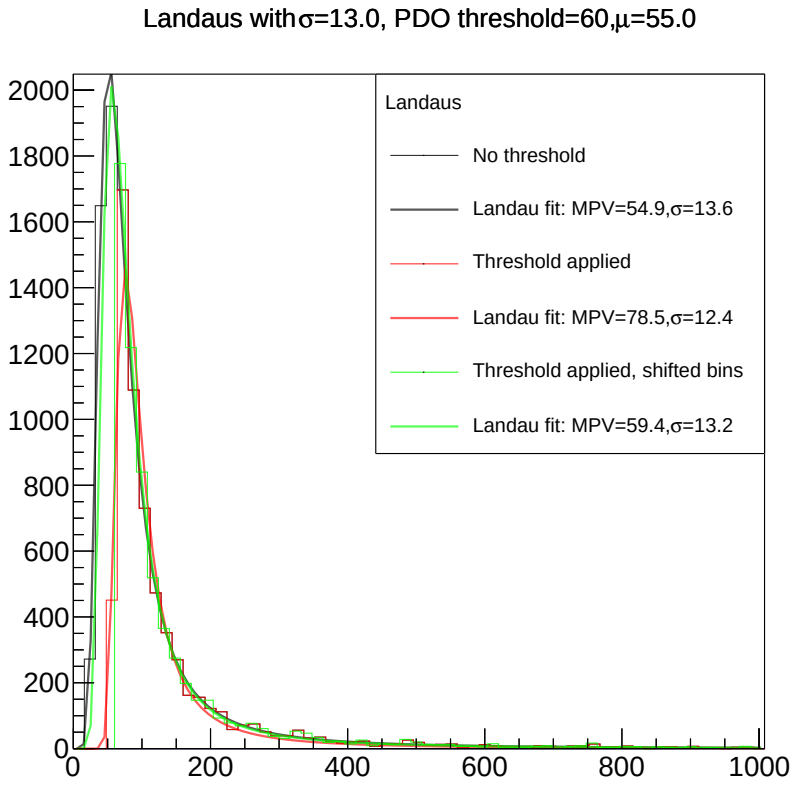

Figure A.3: Three histograms filled with from the same Landau distribution with μ =55 and σ =13. The histogram bins were 16 x-values wide. The green and red histograms are filled by only selecting the generated Landau values above a threshold of 60, while the black histogram was filled with all 10,000 generated Landau values. The lower edge of the first bins for the red and black histograms is 0 while the first bin of the green histogram has a lower edge of 60. Each histogram was fit to a Landau.

histogram with no threshold (black). The generated Landau values that approach the threshold (from the right) lie within the centre of the first non-zero bin of the red histogram. As a result, the rising edge and peak of the Landau distribution is split over two bins, the first of which is below threshold and therefore not digitized, as opposed to the green histogram, where the peak of the distribution is captured by the first bin.

The Landau fits are very sensitive to the first non-empty bins of the histogram, as they describe its rising edge. The fits for the histograms binned by the threshold returned MPVs that approached the μ values that generated the distributions. The MPVs from Landau fits on the three histograms with the same threshold (60) over multiple values of μ are shown in Figure A.4. The MPV vs μ relationship for the

histogram with no threshold is linear and the MPV and μ are approximately equal. For the histogram with the same binning but a threshold on the lower values, the fitted MPVs for the Landau distributions that peak below the threshold are much higher than those from the corresponding histogram with the lowest bin beginning at the threshold.

The implications of these models is that the fits are very sensitive to the first bin of the distribution and that while the histogram that begins at the threshold has Landau fits that do not completely reconstruct the 'true' shape of the distribution, it returns much closer approximations of the location parameters. The 'shifted' histograms are better at reconstructing Landau distributions accurately that have peaks above the threshold.

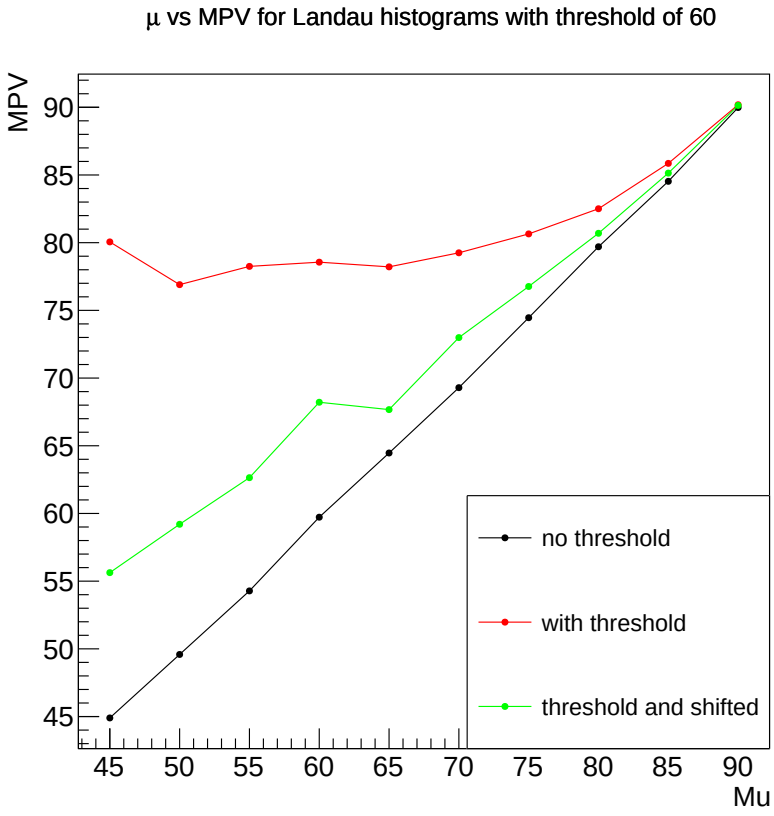

Figure A.4: MPV vs location parameter μ, with MPVs fit on histograms filled with pseudo-random values following Landau distributions with $\sigma = 13$. The black and red points correspond to Landau fits on histograms that are binned in 16 count-wide bins from 0 to 1008. The green points are for histograms that have 16 count-wide bins beginning at the threshold of 60. The histograms corresponding to the red and green points were filled only with generated values that were above the threshold.

A.3 Alternatives to Landau Distributions

The Landau fits of the raw PDO distributions from high background rate runs were poor, with typical χ^2/n from the fits on the order of 100 (before applying cuts or modifications to the binning). The gamma background has a different energy distribution than a minimum ionizing particle, which results in a different distribution of charge deposition which, in turn, would change the raw PDO distribution. For reference, the Landau distribution [32] is given by

$$\phi(\lambda) = \frac{1}{2\pi i}\int_{\sigma-i\infty}^{\sigma+i\infty} e^{u\ln u+\lambda u}du, \text{ for } \sigma \geq 0 \tag{A.2}$$

In order to compensate for this gamma background, we considered alternative fit models, with the aim of describing the combined muon and gamma signal distributions. While the Landau distribution is a model for the energy deposition of charged particles traversing a thin detector, if the sTGC module was a 'thick' material for gamma rays, then the Landau distribution would not be the correct model. The Vavilov distribution is the generalization of the Landau distribution, given by

$$p(\lambda_L, \kappa, \beta^2) = \frac{1}{2\pi i}\int_{c-i\infty}^{c+i\infty} \phi(s)e^{\lambda_L s}ds \tag{A.3}$$

Where $\phi(s)$ is a function of λ_L ,κ, and β^2, given by

$$\phi(s) = \exp(\kappa(1+\beta^2\gamma))\exp(s\ln\kappa + (s+\beta^2\kappa)(\int_0^1 (1-e^{-st/\kappa})/t)dt - \gamma) \tag{A.4}$$

Where $\gamma = 0.5772\ldots$ is Euler's constant [33]. While the distribution approaches a Landau[2] as $\kappa \to 0$ it is a much more complicated function and requires tuning the parameters in order to fit to the data. The fits were created using the probability density function (PDF) calculated by the ROOT VavilovFast class, where the parameters κ and β^2 are constrained such that $0.01 \leq \kappa \leq 12$ and $0 \leq \beta^2 \leq 1$. The PDF $p(\lambda_L, \kappa, \beta^2)$ had to be calculated for every tested parameter value generated in the fitting process, which is computationally expensive. In Figure A.5, an example of the PDO distribution fit to a Vavilov function is shown. The fit does not match either the peak or the tails well, meaning that the model is an extremely poor candidate for describing the combined signal and background.

[2]The Vavilov distribution approaches a Gaussian for large values of κ.

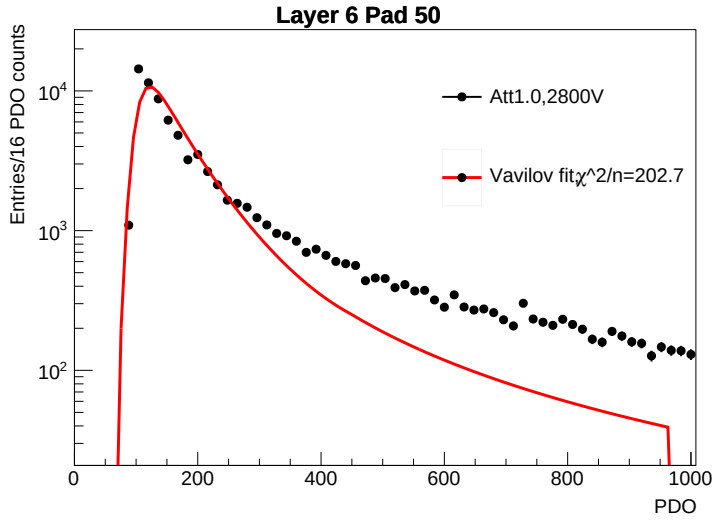

Figure A.5: Raw PDO distribution for a single pad with source on fit to a Vavilov function. The function does not match the peak or tail well and has quite a large χ^2/n. The lower edge of the first bin of the histogram is the pad's threshold.

With a similar motivation of viewing the sTGC as a thicker detector to gamma rays, we also considered a convolution of a Landau and Gaussian, following the example given in [34]. The result of the fit on the PDO distribution of one pad with high background data is shown in Figure A.6. The convolution also did not well describe the distribution. The convolution does not match the peak or tail well and has quite a large χ^2/n and was not further considered as a model.

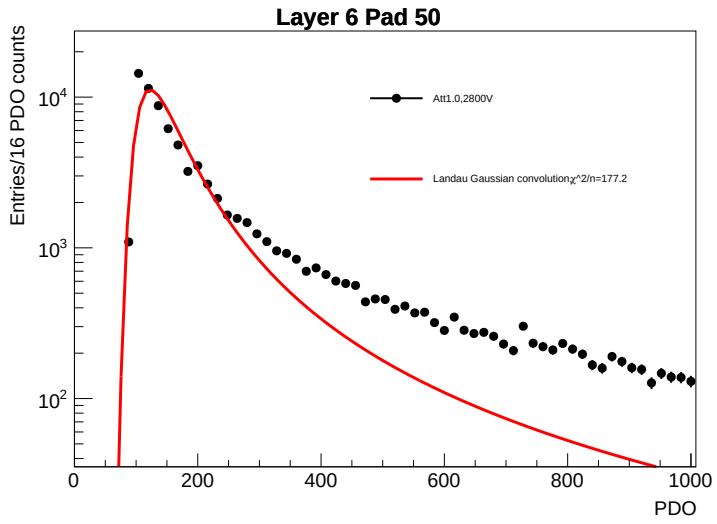

Figure A.6: Raw PDO distribution for a single pad with source on, fit to a convolution of a Landau and Gaussian. The lower edge of the first bin of the histogram is the pad's threshold.